

High Field Magnetic Resonance Facility

A significant portion of research conducted in the High Field Magnetic Resonance Facility (HFMRF) focuses on developing a fundamental, molecular-level understanding of biochemical and biological systems and their response to environmental effects. A secondary focus is in materials science and catalysis and the chemical mechanisms and processes that operate in these areas. Resident and matrixed research staff within this facility offer expertise in the areas of structural biology, solid-state materials characterization, and magnetic resonance imaging (MRI) techniques.

Local research activities include determining the structure of large molecular assemblies such as proteins, DNA (normal and damaged), and RNA complexes as a cellular response to chemical or radiological insults; determining conformational changes in membrane protein complexes involving metal clusters as monitored by pulsed electron paramagnetic resonance (EPR); nuclear magnetic resonance (NMR)-based structural and functional genomics; multi-nuclear detection and catalyst and materials characterization via solid-state techniques; non-invasive biological imaging, integrated magnetic resonance and confocal microscopy, and slow-spinning NMR to study cell systems.

Since the W.R. Wiley Environmental Molecular Sciences Laboratory (EMSL) opened in October 1997, the HFMRF has operated one of EMSL's high-volume experimental user facilities in support of local and external user research programs. During FY 2003, HFMRF supported 121 projects in which 154 external scientists used the NMR spectrometers.

The research interests of the scientific staff include some of the most exciting areas in modern molecular biology and biochemistry:

- **Structural/Functional Genomics.** Determination of three-dimensional structures of DNA, RNA, proteins, and enzymes and their intermolecular associations. Particular interests and collaborations exist relative to protein fold classification and sequence-structure-fold relationships.

Instrumentation & Capabilities

NMR

- 900-MHz NMR (operational in 2004)
- 800-MHz NMR
- 750-MHz NMR
- 600-MHz NMR (2 systems)
- 500-MHz, wide bore NMR (2 systems, 1 delivered in May 2002 – now operational for MRI)
- 500-MHz NMR (2 systems)
- 400-MHz, wide bore NMR
- 300-MHz, wide bore NMR (2 systems)

EPR

- EPR Spectrometer with ENDOR/ELDOR capability

Additional Capabilities

- Combined optical and magnetic resonance microscope
- Low-temperature probes for metallo-protein chemistry and structure
- Virtual NMR capability enabling use and collaboration with EMSL scientists for remote users via secure shell over the internet

- **Biomolecular Complexes.** Understanding the molecular interactions of larger complexes of biomolecules (proteins, DNA, RNA, and mimetic membranes) that are key regulators in cell signaling and growth (e.g., DNA damage recognition and repair processes).
- **Biological Imaging.** Acquisition of imaging and corresponding chemical information in biological samples, with particular interest in development of combined magnetic resonance and optical spectroscopy techniques to observe and elucidate biological processes.
- **Solid State.** Low-gamma nuclei detection, ultra-low-temperature NMR for sensitivity enhancement, and slow-magic-angle-spinning (MAS) methodologies for nondestructive research of cells, tissues, small animals, and bacterial colonies.
- **Measurement Science and Instrumentation Development.** Development and application of novel and unique NMR instrumentation techniques for biological and environmental problems.

Magnetic Resonance Research Capabilities

Varian INOVA 800. The Varian 800 (Figure 1) is an INOVA-based spectrometer and an Oxford 18.8-tesla (T) magnet with a 63-mm, room-temperature bore. This system is capable of high-resolution-liquid and solid-state NMR. There are four RF channels with waveform generators and pulsed-field gradients. The wide-line analog digital converters (ADCs) run at 5 MHz, and the narrow-line ADCs run at a maximum rate of 500 kHz. Available probes include two 5-mm HCN probes with Z gradient for liquids, a 4-mm HXY MAS probe (25-kHz spinning), a 5-mm HX orthogonal powder probe optimized for low-gamma (38 to 65 MHz) nuclides, and a 5-mm HX static low-temperature probe (3.8 to 300 K). Under construction is a 5-mm HX MAS probe (12-kHz spinning).



Figure 1. Varian INOVA 800.

Varian INOVA 750. The Varian 750 (Figure 2) is an INOVA-based spectrometer and an Oxford 17.6-T magnet with a 51-mm, room-temperature bore. This system is capable of high-resolution-liquid and solid-state NMR. There are four RF channels with waveform generators and pulsed-field gradients. The narrow ADCs have a maximum rate of 500 kHz. We currently have two 5-mm HCN probes (Z gradient), a 5-mm HCP probe (Z gradient), a 5-mm HX MAS probe (X tuning range is 321 to 130 MHz; the spinning speed is rated to 12 KHz), and two 5-mm HX MAS probes (15-kHz spinning) with X tuning ranges of 60 to 120 MHz and 30 to 50 MHz.



Figure 2. Varian INOVA 750.

Varian INOVA 600. The Varian 600 (Figure 3) is an INOVA-based spectrometer and an Oxford 14.1-T magnet with a 51-mm, room-temperature bore. This system is capable of high-resolution-liquid NMR. There are four RF channels with waveform generators and pulsed-field gradients. The narrow-line ADCs run at a maximum rate of 500 kHz. We currently have a 5-mm HCN probe with Z gradient and a 5-mm HX probe (X tuning range is 242 to 60 MHz). Delivery of our first 5-mm HCN cryogenic probe is expected in mid-summer 2004.

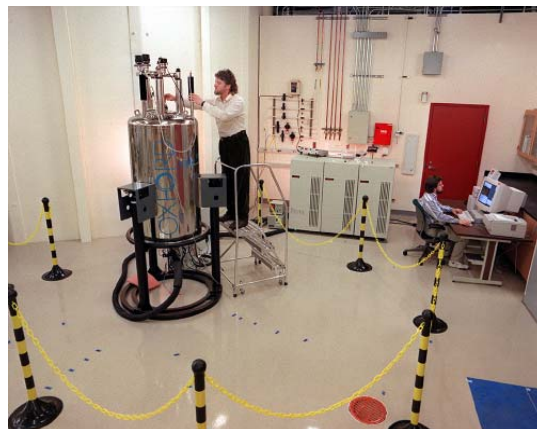


Figure 3. Varian INOVA 600.

Varian Unity 600. The Varian 600 (Figure 4) is a Unity-based spectrometer and an Oxford 14.1-T magnet with a 51-mm, room-temperature bore. This system is capable of high-resolution-liquid NMR. There are three RF channels with waveform generators and pulsed-field gradients. The narrow-line ADCs run at a maximum rate of 500 kHz. We currently have a 5-mm HCN probe with Z gradient and a 5-mm HX probe (X tuning range is 242 to 60 MHz).



Figure 4. Varian Unity 600.

Varian Unity+ 500 Wide Bore. The Varian 500 Wide Bore (Figure 5) is a Unity-based spectrometer and an Oxford 11.7-T magnet with an 89-mm room-temperature bore. This system is capable of solid-state NMR, micro-imaging, and small-animal MRI. There are three RF channels with waveform generators. The wide-line ADCs run at 5 MHz. This year, we upgraded the shim set to a 23-channel RRI system, which should improve magnetic field homogeneity around all samples. We currently have a 5-mm orthogonal powder probe, 5-mm HXY MAS probe (15-kHz spinning), a 7-mm HX MAS probe (10-kHz spinning), an HX single-crystal probe, a ^1H CRAMPS probe, a micro-coil imaging probe, a 40-mm imaging probe, and a static HX low-temperature probe (2 to 300 K).



Figure 5. Varian Unity+ 500 Wide Bore.

Bruker Avance 500 Wide Bore. The Bruker Avance 500 Wide Bore (Figure 6) is a micro-imaging system using an 89-mm vertical room-temperature bore. The system is capable of imaging mice and also has high-resolution liquid magnetic resonance capabilities with a Bruker 10-mm QNP probe. This liquid probe has a ^1H outer coil and an inner coil that is switchable among ^{13}C , ^{31}P , and ^{19}F with no gradients. The system is equipped with a combined confocal and magnetic resonance microscope capable of monitoring single layers of eukaryotic cells in a perfusion system simultaneously with both modalities.



Figure 6. Bruker Avance 500 Wide Bore.

Varian/Chemagnetics Infinity 500. The Chemagnetics 500 (Figure 7) is an Infinity-based spectrometer and an Oxford 11.7-T magnet with a 51-mm, room-temperature bore. This system is capable of high-resolution-liquid and solid-state NMR. It has three RF channels and is equipped with both 16 and 14 bit ADCs. The solution state probes for this instrument are a 5-mm HCN gradient probe, a 5-mm DB gradient probe (X tuning range is 208.1 to 49.5 MHz), and a 10-mm HX probe (X tuning range is 218.6 to 21.2 MHz). There are two solid-state probes, a 5-mm HX MAS probe (X tuning range is 206.6 to 47 MHz; the spinning speed is rated to 12 KHz) and a 6-mm HX MAS probe (X tuning range is 218.6 to 48.7 MHz, H/F tuning range is 510.6 to 459 MHz; the spinning speed is rated to 9 KHz).

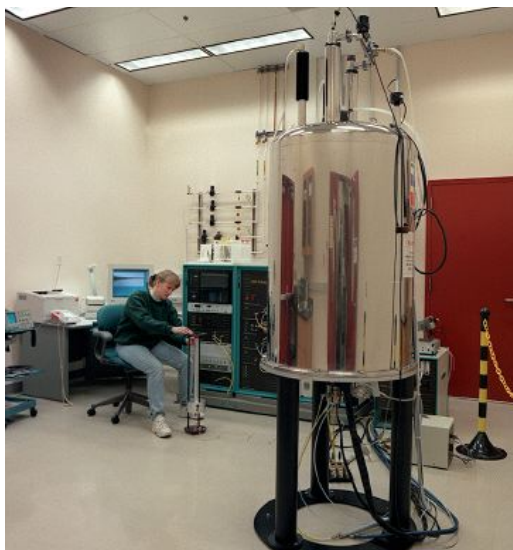


Figure 7. Varian/Chemagnetics Infinity 500.

Varian Unity+ 500 Narrow Bore. The Varian 500 (Figure 8) is a Unity-based spectrometer and an Oxford 11.7-T magnet with a 51-mm, room-temperature bore. This system is capable of high-resolution liquids NMR. There are three RF channels with waveform generators and pulsed-field gradients. We currently have a 5-mm HCN probe with Z gradient and a 10-mm HX probe.



Figure 8. Varian Unity+ 500 Narrow Bore.

Varian/Chemagnetics Infinity+ 400. The Varian 400 spectrometer (Figure 9) is an Infinity+-based spectrometer and an Oxford 9.4-T magnet with an 89-mm, room-temperature bore. This system is only used for solid-state NMR. There are two RF channels and a 5-MHz ADC. We currently have a 5-mm HX MAS probe, a 5-mm HX static cryogenic probe (3.8 to 300 K), a 7-mm HX static low-temperature probe (4.2 to 400 K), and a 10-mm HX DAS probe. All of the Unity+ 500 wide-bore broadband probes may be used in single-channel mode.



Figure 9. Varian/Chemagnetics Infinity+ 400.

Varian/Chemagnetics Infinity 300.

The Chemagnetics 300 (Figure 10) is an Infinity-based spectrometer and an Oxford 7.02-T magnet with an 89-mm room-temperature bore. This system is capable of high-resolution-liquid and solid-state NMR. It has three RF channels and is equipped with both 16 and 14-bit ADCs. The solution-state probes for this instrument are a 5-mm HX probe and a 10-mm HX probe. The solids probes are a 7.5-mm HX MAS probe (X tuning range is 136.7 MHz to 29.5 MHz; H tuning range is 274.7 to 349.1 MHz; spin rate is rated to 7 Hz) and a 5-mm HXY MAS probe (X tuning range is 129 to 57.4 MHz; Y tuning range is 85.1 to 21.2 MHz; spin speed is rated to 12 KHz).



Figure 10. Varian/Chemagnetics Infinity 300.

Varian Unity+ 300. The Varian 300 (Figure 11) is a Unity-based spectrometer and an Oxford 7.04-T magnet with an 89-mm, room-temperature bore. This system is capable of solid-state NMR, micro-imaging, and small-animal MRI. There are two RF channels with wide-line ADCs running at 5 MHz. We currently have a 7-mm HX MAS probe (10-kHz spinning), an HX single-crystal probe, a ^1H CRAMPS probe, a single-tuned DOR probe, an HX 5-mm, low-temperature MAS probe (35 to 300K, 12-kHz spinning), a 7-mm HX high-temperature probe (-100 to 500°C, 7-kHz spinning), a microscopy probe, and a 40-mm imaging probe.



Figure 11. Varian Unity+ 300.

Bruker Pulsed EPR/ENDOR/ELDOR Spectrometer. The EPR/ENDOR work focuses on the development and application of pulsed, two-dimensional methods for electronic structure and distance determinations in biological macromolecules and materials. The spectrometer (Figure 12) consists of a Bruker 380E pulsed EPR spectrometer with pulsed ENDOR. It has been modified to include pulsed ELDOR capabilities.



Figure 12. Bruker pulsed EPR/ENDOR/ELDOR spectrometer.

Upgrades

900-MHz NMR Magnet

The 900-MHz, wide bore NMR magnet (Figure 13) was delivered to EMSL in March 2002 after nearly 10 years of development effort. The magnet was designed and manufactured by Oxford Instruments (Oxford, United Kingdom). It comprises more than 200 miles of specially formulated superconducting wire, weighs over 16 tons, and operates at a field of 21.15 T with 27 MJ of stored energy. Magnet installation, commissioning, stabilization, and testing activities have now been conducted. The 900-MHz NMR capability will be made available to users in mid-2004, enabling enhanced structural studies of biological and environmental molecules and systems.



Figure 13. 900-MHz NMR magnet.

Solid-State NMR Probe Development

Researchers from the HFMRU, along with resident research staff members, are developing unique solid-state probes. One of these unique probes, a cryogenic solid-state NMR probe, is shown in Figure 14, along with its developers. Probe development is taking place for many of the facility's magnets, and currently is expanding to the 21.15-T, 18.8-T, 17.6-T, and 11.75-T magnets. Currently, we have



Figure 14. Cryogenic solid-state NMR probe and its developers.

built two HX static probes capable of cross-polarization (CP) using a cross-coil design for the 18.8-T system. One probe is optimized for low gamma (30 to 50 MHz), which has been implemented to study ^{99}Ru and ^{25}Mg projects. The second probe is optimized for medium gamma (60 to 120 MHz), and has been used to study $^{35/37}\text{Cl}$ and ^{91}Zr projects. This cross-coil design was successfully used on a prototype static CP HX probe for the 21.15-T magnet system. Based on this success, we plan to build a triple-resonance probe for this state-of-the-art system. Two 5-mm CP/MAS (low- and medium-gamma) probes were built for the 17.6-T spectrometer, and new probes are planned for an 11.75-T spectrometer as user needs arise. For the cryogenic static probes that routinely operate at 10 K, application of a third-generation design on the 18.8-T magnet has decreased the experiment time required from 11 hours (previously required on a 9.39-T magnet system) to 1 hour.

Second-Generation Combined Magnetic Resonance and Optical Microscope

Two microscopes for studying live cells simultaneously with magnetic resonance and laser-scanning confocal fluorescence microscopy are housed in the EMSL NMR User Laboratory at Pacific Northwest National Laboratory (Figure 15). Both systems are capable of detecting red and green fluorescence excited with a 588-nm laser that focuses light on an integrated cell culture chamber located at the center of an 11.7-T, vertical, wide-bore (89-mm) magnet. One microscope exploits a Varian Unity+ console for controlling magnetic resonance data acquisition, and a newer microscope, developed in 2003, employs a Bruker Avance imaging spectrometer. The optics for the former are characterized by a longer focal length that is ideal for studying large single cells or small-cell agglomerates with diameters under a millimeter. The newer microscope has a shorter focal length and improved brightness for higher resolution studies of monolayer cell cultures or microbial biofilms with a thickness of less than a few hundred microns. All cell culture sample chambers are temperature-regulated and include integrated plumbing for delivering fresh culture media.

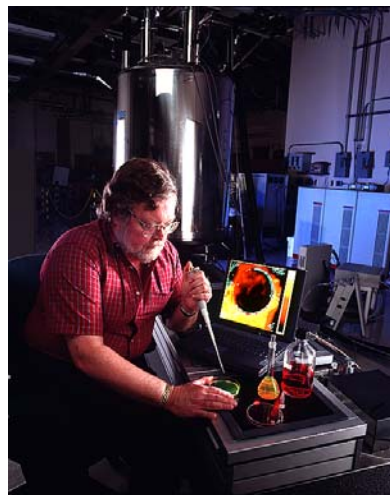


Figure 15. Second-generation combined magnetic resonance and optical microscope.

Linux Cluster and Silicon Graphics, Inc. Computer Programs

A new Linux-based, 24-node cluster is available to users and runs the Accelrys suite. Other computer systems are an 8-CPU SGI Origin 2000 and 4-2 CPU SGI Octanes. Typical programs running on each SGI include NMR Pipe for data processing, NMR View/NMR Draw, Felix for data viewing and manipulation, and Simpson for simulating solid-state line shapes. HADDOCK (by Alexandre Bonvin, Utrecht University, Padualaan, Utrecht, The Netherlands, and co-workers) is available for modeling/calculating the docking of protein-protein complexes.

Structural Genomics of Eukaryotic Model Organisms

JM Aramini,^(a) JR Cort,^(b) TA Ramelot,^(b) CH Arrowsmith,^(c) MA Kennedy,^(b) and GT Montelione^(a)

(a) CABM, Rutgers University, Piscataway, New Jersey

(b) Pacific Northwest National Laboratory, Richland, Washington

(c) University of Toronto, Toronto, Ontario, Canada

The Northeast Structural Genomics Consortium (NESG), a pilot project funded by the National Institutes of Health (NIH) Protein Structure Initiative, focuses on evaluating the feasibility, costs, economies of scale, and value of structural proteomics. The primary goal of our project is to develop integrated technologies for high-throughput (htp) protein production and three-dimensional structure determination by x-ray crystallography and nuclear magnetic resonance (NMR) spectroscopy. Our targets include members of large protein families for which no three-dimensional structural information is available. We prioritize protein families with representatives in human and higher eukaryotic genomes and their homologs in bacteria and archaea. To date, the NESG has submitted more than 90 new protein structures to the Protein Data Bank (PDB), approximately half of which were elucidated by NMR spectroscopy. To this end the High Field Magnetic Resonance Facility in the W.R. Wiley Environmental Molecular Sciences Laboratory (EMSL) has played a key role in this productivity. In 2003, NMR data collected at EMSL across the entire NESG directly resulted in a total of seven new NMR solution structures submitted to the PDB (1RZW, 1R57, 1RQ6, 1Q48, 1NXI, 1NYN, and 1NY4) with three others in refinement, and six assignment and structure publications (Zheng et al. 2003; Ramelot et al. 2003a, 2003b; Pineda-Lucena et al. 2003; Aramini et al. 2003; Wu et al. 2003). In addition to NMR data required for a complete structure analysis (typically 4 to 6 weeks of multidimensional NMR experiments per protein), EMSL has also been a valuable resource for the collection of high-field nuclear Overhauser enhancement spectroscopy (NOESY) data for structure refinement of several NESG targets, as well as relaxation data to probe the dynamics of proteins in solution and ligand binding assays. In the following sections, we highlight three NMR structures solved in 2003, each emanating from data collected at EMSL.

Vibrio cholerae Protein VC0424

The 124-residue *Vibrio cholerae* protein, VC0424, is a member of a conserved family of bacterial proteins of unknown structure and function. The solution NMR structure of VC0424 (Ramelot et al. 2003a) features an open-faced α - β sandwich with an overall α - β - α - β - α - β topology (Figure 1a). One layer is composed of the three α -helices, while the other layer consists of four anti-parallel β -sheets. This fold is a variation of the common ferredoxin-like β - α - β - α - β fold, the main difference being the long α -helix at the N-terminus of VC0424. Several conserved residues among VC0424 and its homologs cluster on the β -sheet face of the protein, which interestingly is recognized as a “supersite” for ligand binding in ferredoxin-like folded proteins.

S28E Ribosomal Protein from Pyrococcus horikoshii

The 71-residue S28E ribosomal protein from the 30S ribosomal unit of the archaean *Pyrococcus horikoshii* is a member of a conserved ribosomal protein domain family of unknown

function in archaea and eukaryotes. The structure of S28E (Aramini et al. 2003) is characterized by a four-stranded β -sheet with a classic Greek-key topology and is a variant of the classic β -barrel OB-fold found in many oligonucleotide and oligosaccharide binding proteins (Figure 1b). The electrostatic surface of S28E exhibits positive and negative patches on opposite sides, the former constituting a putative binding site for RNA. The 13 C-terminal residues of the protein, which contains a consensus sequence motif that is the signature of the S28E protein family and is predicted to be α -helical, is unstructured in solution. The solution structure of S28E is highly homologous to that of the related S28E protein from *Methanobacterium thermoautotrophicum*, solved concurrently within the NESG also using NMR data acquired at EMSL (1NE3; Wu et al. 2003).

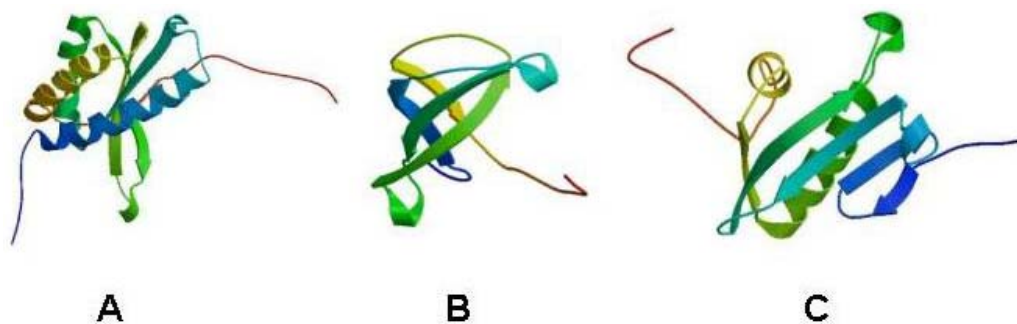


Figure 1. Recent solution NMR structures determined using NMR data collected at EMSL. (A) VC0424 from *V. cholerae* (1NXI; Ramelot et al. 2003a). (B) S28E from *P. horikoshii* (1NY4; Aramini et al. 2003). (C) MW2441 from *S. aureus*. With the aid of automated assignment and structure determination software, the structure of S28E was deposited just 50 days after the start of NMR data collection.

***Staphylococcus aureus* Protein MW2441**

The MW2441 protein from *Staphylococcus aureus* is a 103-residue protein of unknown function that has sequence homologs in several eukaryotes and bacteria. The solution NMR structure of MW2441 revealed that the protein adopts an α/β fold similar to the acetyl-CoA binding domain of GCN5-like N-acetyltransferases (Figure 1c). Moreover, the location of a cofactor binding site involving a conserved cysteine was inferred by comparison of this structure to a crystal structure of an N-acetyltransferase in complex with acetyl-CoA. The N-acetyltransferase activity of this protein was subsequently confirmed by chemical shift perturbation mapping with a sample to which acetyl-CoA had been added. Thus, this structure provides insight into the previously unknown biological function of a protein, namely that MW2441 is a GCN5-like N-acetyltransferase.

Other Recent Structures

Other structures of NESG targets purified at Rutgers University have been also determined in recent months using NMR data acquired at EMSL. These include 1) the IscU protein from *Haemophilus influenzae* (1Q48), which is part of an exciting super-family of proteins that are intimately involved in iron-sulfur cluster biosynthesis across all kingdoms (structures of several of these proteins have been recently solved in the NESG), and 2) the AF2095 hypothetical protein from *Archaeoglobus fulgidis* (1RZW).

References

- Aramini JM, YJ Huang, JR Cort, S Goldsmith-Fischman, R Xiao, LY Shih, CK Ho, J Liu, B Rost, B Honig, MA Kennedy, TB Acton, and GT Montelione. 2003. "Solution NMR Structure of the 30S Ribosomal Protein S28E from *Pyrococcus horikoshii*." *Protein Science* 12:2823-2830.
- Pineda-Lucena A, JC Liao, JR Cort, A Yee, MA Kennedy, AM Edwards, and CH Arrowsmith. 2003. "A Novel Member of the Split $\beta\alpha\beta$ Fold: Solution Structure of the Hypothetical Protein YML108W from *Saccharomyces cerevisiae*." *Protein Science* 12:1136-1140.
- Ramelot TA, JR Cort, AA Yee, A Semesi, AM Edwards, CH Arrowsmith, and MA Kennedy. 2003a. "Solution Structure of the Yeast Ubiquitin-Like Modifier Protein Hub1." *Journal of Structural and Functional Genomics* 4:25-30.
- Ramelot TA, S Ni, S Goldsmith-Fischman, JR Cort, B Honig, and MA Kennedy. 2003b. "Solution Structure of *Vibrio cholerae* Protein VC0424: A Variation of the Ferredoxin-Like Fold." *Protein Science* 12:1556-1561.
- Wu B, A Yee, A Pineda-Lucena, A Semesi, TA Ramelot, JR Cort, JW Jung, A Edwards, W Lee, MA Kennedy, and CH Arrowsmith. 2003. "Solution Structure of Ribosomal Protein S28E from *Methanobacterium thermoautotrophicum*." *Protein Science* 12:2831-2837.
- Zheng D, JR Cort, Y Chiang, T Acton, MA Kennedy, and GT Montelione. 2003. " ^1H , ^{13}C , and ^{15}N Resonance Assignments for Methionine Sulfoxide Reductase B from *Bacillus subtilis*." *Journal of Biomolecular NMR* 27:183-184.

Post-Mortem Energy Metabolism and Water Characteristics in Rabbit Muscle Longissimus Studied by Dynamic Slow-Speed MAS NMR Spectroscopy and Relaxometry

HC Bertram,^(a) JZ Hu,^(b) DN Rommereim,^(c) RA Wind,^(b) and HJ Andersen^(a)

(a) Danish Institute of Agricultural Sciences Research Centre, Foulum, Denmark

(b) Pacific Northwest National Laboratory, Richland, Washington

(c) W.R. Wiley Environmental Molecular Sciences Laboratory, Richland, Washington

During the conversion of living muscle to meat for human consumption, several biochemical and biophysical processes take place that determine the meat quality. Nuclear magnetic resonance (NMR) methodologies are very attractive for studying these processes as they allow non-invasive and continuous measurements of the on-going processes in muscles. Recently, the phase-altered spinning sidebands (PASS) technique, originally developed for solid-state NMR (Antzutkin et al. 1995), was modified for studies of biological objects (Wind et al. 2001). This technique separates the spinning sidebands from the isotropic center band spectrum, and can be applied at spinning rates as low as 40 Hz in biological samples, thus preventing structural damage of the tissue. Therefore, the technique potentially can be used to study post-mortem processes in intact muscles. In the present project, the post-mortem course in rabbit muscle biopsies were followed by dynamically performing a combination of ^1H PASS NMR metabolite spectroscopy, single-pulse ^{31}P NMR metabolite spectroscopy, and ^1H water T2 measurements. Also, half the rabbits were administered adrenaline before sacrifice, thus depleting muscle glycogen stores, which prevents formation of lactate post-mortem (Bendall and Lawrie 1962). The effect that administering adrenaline might have on the various NMR results has been investigated. Figure 1 shows typical ^{31}P spectra recorded on a sample from an adrenaline-treated animal at 15 minutes post-mortem (A) and on a sample from a control animal at 15 minutes (B), 1.5 hour (C), and 20 hours (D) post-mortem. Resonances from phosphomonoesters (PME) (~ 7 ppm), inorganic phosphate (Pi) (~ 5 ppm), phosphocreatine (PCr) (0 ppm), and γ -, α -, and β -phosphate groups in nucleoside triphosphate (NTP) (~ -6.5 , -11 , and -20 ppm) are observed. During the measuring period, a decrease in the PCr concentration and subsequently a deprivation of NTP were seen. The initial level of NTP was found to be significantly higher in control samples than in samples from adrenaline-treated animals.

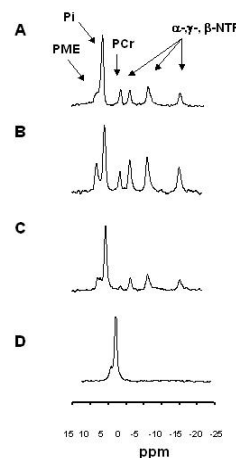


Figure 1. ^{31}P spectra recorded on a sample from an adrenaline-treated animal at 15 minutes post mortem (A), and on a sample from a control animal at 15 minutes (B), 1.5 hours (C), and 20 hours (D) post-mortem.

Figure 2a shows a typical ^1H spectrum obtained on a static muscle sample, and Figure 2b shows the centerband of a ^1H two-dimensional PASS spectrum obtained on a muscle sample at a sample spinning rate of 40 Hz. A tremendous improvement in resolution is obtained

using the PASS technique, allowing detection of several metabolites in the muscle tissue. In part, based on the results of TOCSY experiments (data not shown), the resonances were tentatively identified as described in the Figure 2 caption. During the post-mortem period, noticeable changes were observed in the 6.5 to 9 ppm region (Figure 3). Two histidine peaks are observed in the 8.3 to 8.6 ppm region; one of these peaks had a different chemical shift in the control and the adrenaline-treated animals. This shift can be explained by a difference in pH between the two types of samples. In the control sample a new peak at 6.8 ppm appeared during the post-mortem period. The origin of the 6.8-ppm peak remains a matter of dispute. The 6.8-ppm peak was recently reported to appear occasionally in muscles during exercise (Damon et al. 2003). The peak was suggested to reflect a splitting of the already existing 7.2 ppm histidine C-8 proton peak, and the presence of the two resonances were suggested to reflect the presence of histidine in oxidative and glycolytic muscle fibres, respectively. In contrast, Arus et al. (1984) ascribed the existence of the 6.8-ppm peak to the amino protons in creatine. The fact that the peak in the present study was absent initially post-mortem and in adrenaline-treated muscles reveals that its appearance is pH-dependent. This explains the rare observations of the peak and also matches the fact that it appeared during exercise of muscles (Damon et al. 2003) when pH decreases as a consequence of lactate accumulation. An

alternative explanation could be that the 6.8-ppm peak originates from tyrosine, as two of the aromatic protons have a chemical shift in this range (Sharma et al. 2003). Further studies should be accomplished to identify the origin of the 6.8-ppm peak.

It is anticipated that the results of our research will contribute to further elucidation of the fundamental biochemical and bio-physical processes taking place post-mortem of importance for meat quality.

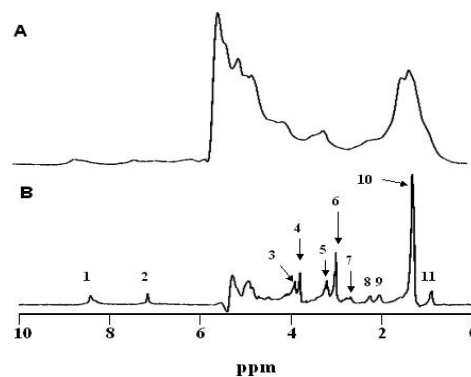


Figure 2. Examples of the water-suppressed ^1H NMR metabolite spectrum of a control muscle sample 24 hours post-mortem obtained on a static sample (A), and with 40-Hz magic angle spinning using the PASS technique (B). The 10 main resonances observed in Figure 2B are assigned as follows: 1) (~8.5 ppm): histidine 6-CH; 2) (7.2 ppm): histidine 8-CH; 3) (3.9 ppm): creatine methylene; 4) (~3.8 ppm): 2-CH of amino groups; 5) (3.2 ppm): choline/pcho methyl; 6) (3.0 ppm): creatine methyl 7) (~2.7 ppm): Lipid =CH-CH₂-CH=; 8) (2.2 ppm): Lipid (OOC-CH₂-); 9) (2.0 ppm): lipid (CH₂-CH₂-CH=); 10) (~1.3 ppm): lactate methyl and lipid (CH₂)_n, 11: lipid methyl.

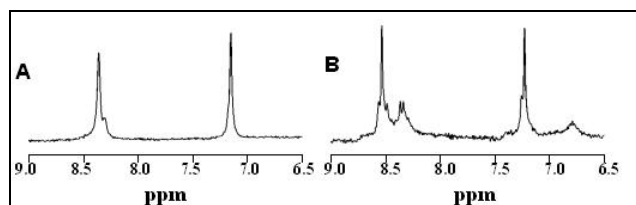


Figure 3. Typical examples of ^1H PASS spectra in the 6.5 to 9 ppm region acquired on a muscle sample from an adrenaline-treated animal at 20 minutes post-mortem (A), and on a muscle sample from a control animal at 20 hours post-mortem (B).

References

- Antzutkin ON, SC Shekar, and MH Levitt. 1995. "Two-Dimensional Side-Band Separation in Magic-Angle-Spinning NMR." *Journal of Magnetic Resonance Series A* 115(1):7-19.
- Arus C, M Barany, WM Westler, and JL Markley. 1984. "¹H NMR of Intact Muscle at 11-T." *FEBS Letters* 165(2):231-237.
- Bendall JR and RA Lawrie. 1962. "The Effect of Pretreatment with Various Drugs on Post-Mortem Glycolysis and the Onset of Rigor Mortis in Rabbit Skeletal Muscle." *Journal of Comparative Pathology and Therapeutics* 72:118-130.
- Damon BM, AC Hsu, HJ Stark, and MJ Dawson. 2003. "The Carnosine C-2 Proton's Chemical Shift Reports Intracellular pH in Oxidative and Glycolytic Muscle Fibers." *Magnetic Resonance in Medicine* 49(2):233-240.
- Sharma U, S Atri, MC Sharma, C Sarkar, and NR Jagannathan. 2003. "Skeletal Muscle Metabolism in Duchenne Muscular Dystrophy (DMD): An In-vitro Proton NMR Spectroscopy Study." *Magnetic Resonance Imaging* 21(2):145-153.
- Wind RA, JZ Hu, and DN Rommerein. 2001. "High-Resolution ¹H NMR Spectroscopy in Organs and Tissues Using Slow Magic Angle Spinning." *Magnetic Resonance in Medicine* 46(2):213-218.

Molecular Structure of Anastellin: An FN3 Fragment with Fibronectin Polymerization Activity

K Briknarová,^(a) ME Åkerman,^(a) DW Hoyt,^(b) E Ruoslahti,^(a) and KR Ely^(a)

(a) The Burnham Institute, La Jolla, California

(b) W.R. Wiley Environmental Molecular Sciences Laboratory, Richland, Washington

Anastellin is a carboxy-terminal fragment of the first FN3 domain from human fibronectin. It is capable of polymerizing fibronectin *in vitro* (Morla et al. 1994), and it displays anti-tumor, anti-metastatic, and anti-angiogenic properties *in vivo* (Yi and Ruoslahti 2001). Identification of structural features responsible for the activity of anastellin may enable development of new anticancer drugs as well as shed light on the mechanism of fibronectin fibrillogenesis. While working towards this goal, we have determined the solution structure of anastellin using nuclear magnetic resonance (NMR) spectroscopy and identified residues critical for its activity (Briknarová et al. 2003).

Anastellin in phosphate-buffered saline at pH 7 was not amenable to NMR structural analysis because its ^1H - ^{15}N HSQC spectrum showed virtually no cross peaks [Figure 1(a)]. To overcome this problem, various conditions and additives were tested. The non-denaturing zwitterionic detergent 3-[(3-chloamidopropyl)dimethylammonio]-1-propane sulfonate (CHAPS) improved spectral quality dramatically at concentrations well below its critical micelle concentration [Figure 1(b)]. Obviously, in solution, anastellin exhibits dynamic fluctuations and conformational exchange, and interaction with CHAPS stabilizes the protein in a particular form that is suitable for NMR structural investigations.

Once appropriate conditions were found, we collected three-dimensional HNCACB, HNCO, C(CO)NH, H(CCO)NH, HCCH-TOCSY, and $^{13}\text{C}/^{15}\text{N}$ -edited nuclear Overhauser enhancement spectroscopy (NOESY) spectra on a 600-MHz NMR spectrometer at the W.R. Wiley Environmental Molecular Sciences Laboratory (EMSL). This data enabled us to establish ^1H , ^{13}C , and ^{15}N resonance assignments and to generate distance restraints for structure calculations. At EMSL, we also acquired a three-dimensional ^{13}C -filtered/ ^{13}C -edited NOESY spectrum that helped us determine the position of CHAPS in the complex (Figure 2).

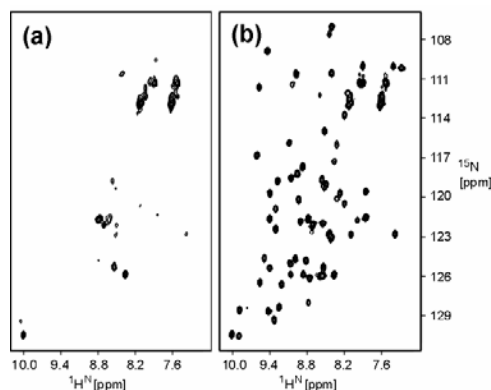


Figure 1. Effect of CHAPS on NMR spectra of anastellin: ^1H - ^{15}N HSQC spectra of 0.7 mM ^{15}N -labeled anastellin (a) in the absence and (b) in the presence of 2 mM CHAPS. All sample conditions, acquisition, processing, and display parameters were identical in the two experiments.

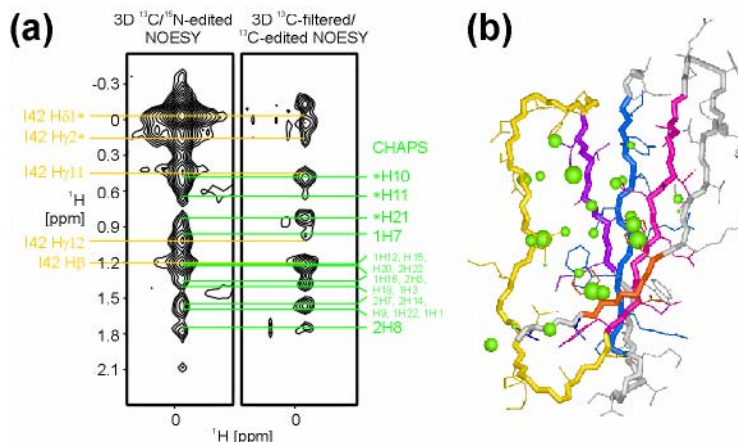


Figure 2. Interaction of anastellin with CHAPS. (a) Cross peaks between I42 Hδ1* and CHAPS in a strip from a three-dimensional ¹³C-filtered/¹³C-edited NOESY spectrum (mixing time 100 ms). A strip from a standard three-dimensional ¹³C-edited NOESY (mixing time 125 ms), which contains strong intra-residual signals, is included for comparison. Chemical shifts of I42 and CHAPS that go through the peaks are indicated on the sides. (b) Distribution of potential CHAPS NOEs observed in a three-dimensional ¹³C-filtered/¹³C-edited NOESY spectrum. Anastellin atoms that display cross peaks at positions of CHAPS chemical shifts are shown as green spheres. The size of the spheres is proportional to the number of NOEs from each atom.

Overall topology of anastellin is very similar to the corresponding region of full-length FN3 domains. However, its hydrophobic core becomes solvent-accessible, and some of its β-strands lose their protection against hydrogen bonding to β-strands from other molecules. These features seem to be relevant for the fibronectin polymerization activity of anastellin and resemble the characteristics of amyloid fibril precursors. We suggest that this analogy is not random and may reflect similarities between fibronectin and amyloid fibril formation (Briknarová et al. 2003).

References

- Briknarová K, ME Åkerman, DW Hoyt, E Ruoslahti, and KR Ely. 2003. "Anastellin, an FN3 Fragment with Fibronectin Polymerization Activity, Resembles Amyloid Fibril Precursors." *Journal of Molecular Biology* 332:205-215.
- Morla A, Z Zhang, and E Ruoslahti. 1994. "Superfibronectin is a Functionally Distinct Form of Fibronectin." *Nature* 367:193-196.
- Yi M and E Ruoslahti. 2001. "A Fibronectin Fragment Inhibits Tumor Growth, Angiogenesis, and Metastasis." *Proceedings of the National Academy of Sciences* 98:620-624.

Nuclear Magnetic Resonance (NMR) Structural Investigations of the Breast Cancer Susceptibility Protein, BRCA1

P Brzovic,^(a) DW Hoyt,^(b) and RE Klevit^(a)

(a) University of Washington, Seattle, Washington

(b) W.R. Wiley Environmental Molecular Sciences Laboratory, Richland, Washington

BRCA1, a breast and ovarian cancer tumor-suppressor protein, supports a number of fundamental cellular processes. Its absence during embryogenesis is lethal. Loss of function in proliferating breast or ovarian epithelial cells can result in the development of cancer. A growing body of literature suggests that BRCA1 interacts with at least 25 different macromolecules to function in processes such as the cellular response to DNA damage, homologous recombination, transcriptional regulation, and, more recently, ubiquitination. A complete picture of the cellular role of BRCA1 requires a detailed understanding of both the function and the structure of the protein and its interacting partners. BRCA1 is a large and complicated protein undoubtedly composed of many functional domains. To date, our structural work has focused on the N-terminal RING domain of BRCA1 in complex with the N-terminal RING domain of BARD1 (Brzovic et al. 2001). Of particular interest is the recent demonstration that BRCA1 functions as an ubiquitin ligase (Brzovic et al. 2003). Formation of the BRCA1/BARD1 RING domain heterodimer is obligatory for this activity. Protein ubiquitination provides a powerful regulatory mechanism for controlling pathways that include cell-cycle progression, transcriptional regulation, and responses to DNA damage. As E3-ligases, RING domains are thought to facilitate the specificity of ubiquitination reactions by forming a multiprotein complex, binding both an ubiquitin conjugating enzyme (E2) covalently activated with ubiquitin and specific proteins targeted for ubiquitination. This work is focused on determining the factors that govern the assembly of this multi-protein complex at the molecular level and that will further our understanding of the molecular mechanism underlying the deleterious structural and functional consequences of BRCA1 cancer pre-disposing mutations.

This system is unique for studying protein-protein interactions by NMR. It involves characterizing the interactions between at least four different protein components: BRCA1, BARD1, an E2 (UbcH5c or UbcH7), and ubiquitin (Ub). The molecular weight of the fully assembled complexes approaches 52 kD. In previous years, we have been able to collect a great deal of data on the individual components of the system. Over the last year, data collected on the 600-, 800-, and 900-MHz NMR instruments in the W.R. Wiley Environmental Molecular Sciences Laboratory (EMSL) have enabled us to begin piecing together the molecular puzzle of this multi-protein complex. Our studies at EMSL uncovered a non-covalent binding site for Ub on a surface of UbcH5c located on a surface far removed from the active site. A single mutation in UbcH5c that disrupts this

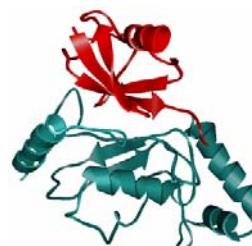


Figure 1. Structure of the non-covalent complex formed between UbcH5c and ubiquitin. Ubiquitin (red) binds to the exposed β -sheet region of UbcH5c (blue-green). The active site of UbcH5c is on the opposite side of the molecule.

interaction is sufficient to eliminate BRCA1-directed, poly-ubiquitin chain formation *in vitro*. Though the affinity of this site for Ub is low ($K_d \sim 300 \mu\text{M}$) data collection on both 800 and 900 MHz instruments at EMSL has been critical for calculating the structure of the UbcH5c-Ub structure (Figure 1.)

During this past year we have also made significant progress toward completing the structure of the BRCA1-BARD1 RING heterodimer in complex with UbcH5c (Figure 2). Although other RING protein-E2 structures have been reported, this complex is catalytically competent and the two proteins appear to associate in a manner substantially different from previous reports. These studies help to delineate factors that govern the specificity of RING(E3)-E2 protein interactions.

Recently, we have been able to generate and collect preliminary spectra on the activated UbcH5c~Ub covalent complex. We plan to characterize this species in much greater structural detail alone and in complex with the BRCA1/BARD1 heterodimer. This is particularly exciting since these complexes have previously not been amenable to detailed structural characterization, which is now made possible by the high-field instruments at EMSL. We anticipate that, during the coming year, these studies will help us further understand the complicated set of interactions between BRCA1 and its partner proteins.

References

Brzovic PS, JR Keefe, H Nishikawa, K Miyamoto, D Fox, M Fukuda, T Ohta, and RE Klevit. 2003. "Binding and Recognition in the Assembly of an Active BRCA1-BARD1 Ubiquitin Ligase Complex." *Proceedings of the National Academy of Sciences* 100:5646-5651.

Brzovic PS, P Rajagopal, DW Hoyt, MC King, and RE Klevit. 2001. "Structure of a BRCA1-BARD1 Heterodimeric RING-RING Complex." *Natural Structural Biology* 10:833-837.



Figure 2. Structure of the BRCA1-BARD1 heterodimer (magenta) in complex with UbcH5c (blue-green). The UbcH5c active site cysteine is highlighted in yellow.

Relaxation Nuclear Magnetic Resonance Imaging (R-NMRI) of Heterogeneous Polymer Aging

B Cherry,^(a) K Minard,^(b) M Celina,^(a) R Clough,^(a) and T Alam^(a)

(a) Sandia National Laboratories, Albuquerque, New Mexico

(b) Pacific Northwest National Laboratory, Richland, Washington

R-NMRI was employed to study the effects of heterogeneous aging of polymeric materials. It is well known that diffusion-limited processes become important in the degradation of materials. A prime example is diffusion-limited oxidation (DLO) processes in polymers. For example, the chemical cross-linking of polymer chains, when aged in an oxygen environment, cause polyurethane materials to harden (Celina et al. 2000). Micro-modulus profiling perpendicular to the surface exposed to oxygen reveals that DLO is occurring. We have recently shown that the NMR spin-spin relaxation time (T_2) measured perpendicular to the oxygen diffusion front can be directly correlated to the modulus of the polyurethane material. By imaging the polymer and measuring T_2 at each voxel, an image can be generated in which the contrast from voxel to voxel is a physical property of the material. This technique allows the heterogeneity of polymer aging to be non-invasively imaged. The R-NMRI experiments were carried out at the W.R. Wiley Environmental Molecular Sciences Laboratory in October 2003 on the Varian Inova 500-MHz instrument and μ -imaging probe.

A 2.5-mm x 2.0-mm x 2.5-mm piece of the polyurethane material was cut from the aged polymer pad to produce a sample in which the DLO process occurred from the top and bottom surfaces inward, Figure 1(a). The surface exposed to oxidation is darker in color. To handle the relatively short T_2 present in the polymer, a three-dimensional constant time imaging (CTI) experiment was performed. This approach allowed the shortest possible imaging sequence and provided minimal signal loss during image collection. Figure 1(b) is a two-dimensional slice through the three-dimensional image where the contrast in the image is the ^1H density.

To measure T_2 for each voxel, a spin echo pre-filter was placed prior to the CTI sequence (Beyea et al. 1998). Three datasets were collected with spin echo encoding times of 0, 300 μs , and 1 ms. The decay of the image intensity with encoding time was used to calculate the T_2 relaxation constant for each voxel, assuming a single exponential.

Figure 2(a) is the T_2 map calculated for the two-dimensional slice in Figure 1(b). The T_2 values are visualized according to the color bar to the left. The T_2 map illustrates the decrease in T_2 at the surface of the polymer due to hardening/cross-linking. The T_2 near

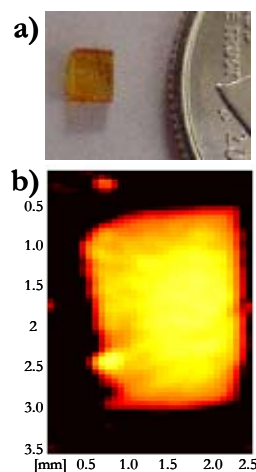


Figure 1. (a) The polyurethane material used in the imaging experiment. The DLO surface is the dark band at the top and bottom of the polymer. (b) Two-dimensional slice through the three-dimensional image taken of the polymer oriented as in (a).

the surface became shorter (the blue-green voxels correspond to shorter T_2 values), while T_2 values in the interior of the sample remain long (no hardening has occurred). Figures 2(b) and 2(c) are histogram plots of the T_2 values measured across the rows and columns of the image. The pronounced arch of the T_2 values measured, depicted in Figure 2(c), reveals that the diffusion-limited reduction in T_2 is caused by the oxygen penetration depth, variations between the individual two-dimensional slices of the full three-dimensional image, and within each slice probe, additional variations of the heterogeneous aging within the polymer.

The preliminary results of this study show the utility of R-NMI to provide valuable insights into the heterogeneous phenomena present in polymer aging. This collaborative user project will result in multiple publications that are currently being written.

References

Beya SD, BJ Balcom, PJ Prado, AR Cross, CB Kennedy, RL Armstrong, and TW Bremner. 1998. "Relaxation Time Mapping of Short T_2^* Nuclei with Single-Point Imaging (SPI) Methods." *Journal of Magnetic Resonance* 135:156-164.

Celina M, AC Graham, KT Gillien, RA Assink, and LM Minier. 2000. "Thermal Degradation Studies of Polyurethane Propellant Binder." *Rubber Chemistry and Technology* 73(4):678-693.

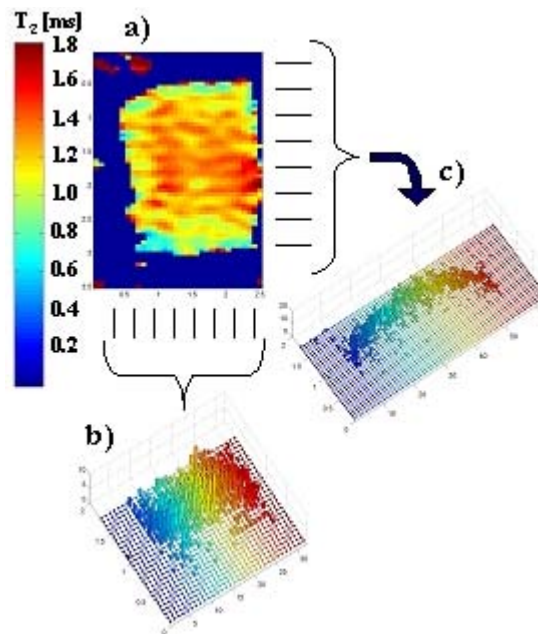


Figure 2. (a) Spin-Spin relaxation time, T_2 , map generated for the two-dimensional slice shown in Figure 1(b). (b) Histogram plot of the T_2 values measured down the vertical columns of the image. (c) Histogram plot of the T_2 values measured across the horizontal rows of the image. The DLO process is clearly depicted from the curvature of the measured T_2 values with depth.

Investigating Molecular Recognition and Biological Function at Interfaces Using Antimicrobial Peptides

ML Cotten,^(a) MN Manion,^(a) and KC Daugherty^(a)

(a) Pacific Lutheran University, Tacoma, Washington

The research presented here begins to explore the principles underlying biological function of peptides and proteins active at interfaces. Specifically, molecular mechanisms of action are examined through the study of membrane-interacting, amphipathic, cationic, antimicrobial peptides (ACAP). Natural ACAPs are water-soluble, cationic, partly hydrophobic, relatively short peptides (6 to 50 residues) that exhibit broad-spectrum antibacterial, fungicidal, hemolytic, virucidal, and tumoricidal activities. The initial targets of ACAPs are believed to be negatively charged microbial membranes. In fact, their amphipathic structures, molecular volumes, and aggregation states in solution and the membrane have been considered important for their interactions with biological membranes. Fully understanding how ACAPs work may involve studying the possible synergy between “multi-hit” mechanisms (i.e., interactions with cellular membranes as well as intracellular components). Overall, there is still much to uncover about the initial interactions of ACAPs with membranes and the events unfolding thereafter. In this respect, understanding the function of ACAPs requires analysis of high-resolution, three-dimensional structures of their membrane-bound states so that relationships can be established between their structural motifs, interactions with biological membranes, activities, and mechanisms of action.

Approaching the study of ACAPs using membrane-mimetic systems has allowed tremendous progress in determining the impact of specific parameters at the molecular level. The ACAPs investigated in this research are piscidins, which were discovered in fish immune mast cells of gills, skin, and gut (Silphaduang and Noga 2001). They are the first ACAPs ever found in the mast cells of animals and are believed to play a crucial, direct role in the fight against many infections. Peculiar features of piscidins include 1) an amidated form, apparently not hemolytic for human red blood cells; 2) a high salt concentration tolerance; 3) highly conserved amino ends; 4) highly cationic states; and 5) a high histidine content.

Solid-state nuclear magnetic resonance (ssNMR) offers major advantages for probing local structure, dynamics, and the precise nature of peptide-lipid interactions under changing conditions (e.g., temperature, hydration, pH). Emerging ssNMR techniques can be performed on site-specific, isotopically labeled, membrane-bound proteins and peptides to measure intermolecular distances and relaxation parameters for the characterization of peptide structure and dynamics. Our strategy includes performing chemical shifts and distance measurements using a number of ssNMR experiments, especially ^{13}C cross-polarization, magic-angle-spinning (CPMAS) and ^{13}C - ^{15}N rotational echo double resonance (REDOR) (Guillion and Schaefer 1989).

To date, site-specific labeled $^{13}\text{C}_i/^{15}\text{N}_{i+4}$ and $^{13}\text{C}_i/^{13}\text{C}_{i+1}$ isotopically labeled piscidins have been synthesized by solid-phase peptide synthesis, purified by high-pressure liquid chromatography, and characterized by mass spectroscopy. Hydrated peptide-lipid samples have then been prepared for ssNMR analysis. Using these samples, the secondary structure is first studied by recording ^{13}C CPMAS isotropic carbonyl chemical shifts along the peptide

backbone in the presence and absence of lipids. The observed ^{13}C chemical shifts suggest that the peptide adopts an α -helical structure in the presence of lipids (Figure 1), as predicted from the peptide amino acid sequence. Concomitantly, we are attempting to measure $^{13}\text{C}_i/^{15}\text{N}_{i+4}$ distances along the peptide backbone using REDOR to determine if hydrogen bonds characteristic of α -helical secondary folds are present in Piscidin 1. Our approach for distance measurements of the hydrated peptide-lipid sample includes a low temperature ($\sim -50^\circ\text{C}$) to quench dynamics problematic at room temperature. Subsequently, we plan to test various pH conditions and lipid types to determine parameters that regulate specificity and activity.

The advanced instruments available to users at the W.R. Wiley Environmental Molecular Sciences Laboratory (EMSL) have been essential to our progress.

References

Gullion T and J Schaefer. 1989. "Rotational-Echo Double-Resonance NMR." *Journal of Magnetic Resonance* 88(1):196-200.

Fernandez VL, JA Reimer, and MM Denn. 1992. "Magnetic Resonance Studies of Polypeptides Adsorbed on Silica and Hydroxyapatite Surfaces." *Journal of the American Chemical Society* 114:9634-9642.

Hirsh DJ, J Hammer, WL Maloy, J Blazyk, and J Schaefer. 1996. "Secondary Structure and Location of a Magainin Analogue in Synthetic Phospholipid Bilayers." *Biochemistry* 35(39):12733-12741.

Lam YH, SR Wassall, CJ Morton, R Smith, and F Separovic. 2001. "Solid-State NMR Structure Determination of Melittin in a Lipid Environment." *Biophysical Journal* 81(5):2752-2761.

Silphaduang U and EJ Noga. 2001. "Antimicrobials: Peptide Antibiotics in Mast Cells of Fish." *Nature* 414:268-269.

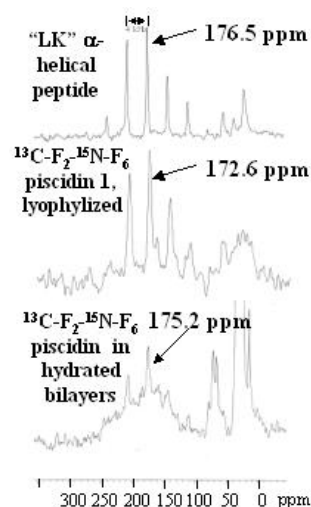


Figure 1. ^{13}C NMR spectra recorded at 125.799 MHz under magic-angle-spinning at a rate of 4 kHz using a triple resonance Doty probe. Spectra were recorded at room temperature except for the spectrum corresponding to the sample in hydrated lipid bilayers (lower spectrum, 1:3 G:PC, ether-linked), which was obtained at -50°C . Isotropic chemical shifts (ppm), indicated by arrows, are referenced to tandem mass spectroscopy assuming that the phospholipid methylene peak appears at 33 ppm for the lipid-containing sample. For the hydrated peptide-lipid sample (bottom spectrum, $\sim 1:30$), the position of the carbonyl isotropic CS at 175.2 ppm is higher than what is observed for the pure peptide, 172.6 ppm, suggesting an α -helical structure (Fernandez et al. 1992; Hirsh et al. 1996; Lam et al. 2001).

Variable-Temperature MAS NMR Spectroscopic Study of Incorporated and Sorbed ^{133}Cs and ^{23}Na in Zeolites

Y Deng,^(a) JJ Ford,^(b) SD Burton,^(b) JB Harsh,^(a) and M Flury^(a)

(a) Washington State University, Pullman, Washington

(b) W.R. Wiley Environmental Molecular Sciences Laboratory, Richland, Washington

Mineral alteration has been observed in sediments underlying high-level radioactive waste storage tanks that have leaked at the U.S. Department of Energy's Hanford Site. The alteration may change sediment properties for incorporation, adsorption, and desorption of pollutants from the waste leaks. Cancrinite, sodalite, Linde Type A (LTA) zeolite, and allophane have been observed in our simulation experiment. The new mineral phases, especially the colloid-sized particles, may facilitate the transport of radioactive nuclides in the vadose zone. Radioactive ^{133}Cs is a major radiation source in the tank waste. Feldspathoids and zeolites contain cages and channels in which Cs^{1+} can exist as ion pairs with OH^{1-} , NO_3^{1-} , NO_2^{1-} , CO_3^{2-} , Cl^{1-} , and SO_4^{2-} . Water in the cages of the minerals may also affect the chemical environment of the cations. In this project, we used variable temperature magic-angle-spinning nuclear magnetic resonance (MAS NMR) to investigate the chemical environment of Cs and Na inside feldspathoids and zeolites (Norby et al. 1998).

We carried out this experiment on a Varian/Chemagnetics Infinity-plus 400 NMR spectrometer at the W.R. Wiley Environmental Molecular Sciences Laboratory. Temperature was varied from 213 K to 498 K, and the rotors were spun at 8 kHz. Cancrinite, sodalite, and LTA zeolite showed different responses to the temperature changes, two examples of which are given in Figure 1. For the sodalite in which Cs was incorporated, the ^{23}Na MAS spectrum recorded at 293 K shows a main peak at -5.7 ppm and a shoulder at around 2.4 ppm [Figure 1(a)]. Decreasing temperature to 213 K causes the peaks to merge to one broader peak. Increasing temperature enhanced the intensity of the 2.4-ppm peak and weakened and shifted the peak at -5.7 ppm. The two peaks were best resolved in the temperature range of 353 to 423 K. Increasing temperature above 448 K caused the collapse of the 2.4-ppm peak. These changes suggest that the chemical environment in sodalite is homogenous for Na at low temperatures. Motion averaging of cations in sodalite does not seem to be the major contributor to the singularity of the NMR peak at low temperatures. Increasing temperature reduced moisture in the cages and likely caused the different chemical environments. We may assign the -5.7-ppm peak to the hydrated Na and the 2.4-ppm peak to the dehydrated Na.

The ^{133}Cs NMR spectra of LTA zeolite [Figure 1(b)] are very different from the spectra of cancrinite or sodalite (data not shown). LTA zeolite has only one narrow peak at different temperatures, thus indicating very homogenous chemical environments or high motion of the Cs in LTA zeolite. We recorded a pattern at 293 K without spinning the rotor [the third spectrum from bottom, Figure 1(b)], and the peak is nearly as narrow as the one recorded with a spin rate of 8 kHz. This narrow peak width suggests that the mobility of cations in LTA zeolite is nearly as high as those in solutions. This is likely the result of the large size of the α -cage in LTA zeolite [Figure 2(b)].

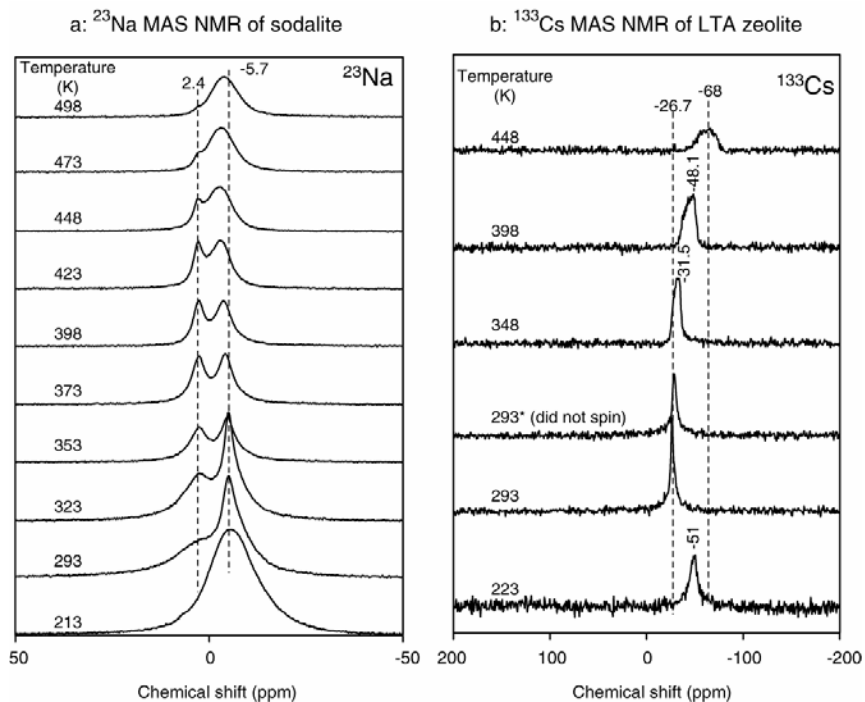


Figure 1. Variable temperature MAS NMR spectra of samples containing Cs. (a) ^{23}Na of sodalite and (b) ^{133}Cs of LTA zeolite. (Na is the dominant cation in both samples.)

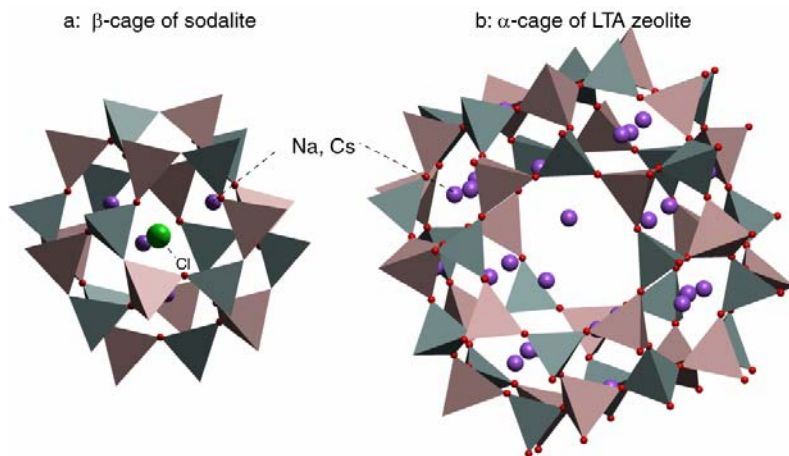


Figure 2. Cages in (a) sodalite and (b) LTA zeolite. LTA zeolite contains both α - and β -cages, but cations stay in the large α -cage, which has more freedom for the migration of cations.

Reference

Norby P, FI Poshni, AF Gualtieri, JC Hanson, and CP Grey. 1998. "Cation Migration in Zeolites: An *In Situ* Powder Diffraction and MAS NMR Study of the Structure of Zeolite Cs(Na)-Y During Dehydration." *Journal of Physical Chemistry B* 102:839-856.

Magic-Angle-Spinning NMR of Highly Radioactive Ceramics: ^{29}Si NMR of Zircons Containing 10 wt% ^{239}Pu and ^{238}Pu

I Farnan,^(a) H Cho,^(b) WJ Weber,^(b) RW Scheele,^(b) NR Johnson,^(a) and A Kozelisky^(b)

(a) University of Cambridge, Cambridge, United Kingdom

(b) Pacific Northwest National Laboratory, Richland, Washington

We have developed a protocol for acquiring magic-angle-spinning nuclear magnetic resonance (MAS NMR) spectra of highly radioactive samples. To our knowledge, this is the first report of such an experiment. These methods have been used to quantify the radiation damage occurring in man-made ceramic samples containing ^{239}Pu and ^{238}Pu . Internal radioactive decay is accelerated in these systems, and they serve as a model for the long-term behavior of potential ceramic radionuclide waste forms.

Naturally occurring zircons (ZrSiO_4) can contain the radioactive elements uranium and thorium at levels up to several thousand ppm. They exhibit a mixed crystalline and amorphous character because of the large number of radioactive decay events that have taken place within them over geological time. MAS NMR measurements can enumerate silicon atoms in the amorphous and crystalline phases and have provided, for the first time (Farnan and Salje 2001), a quantitative measure of the amount of structural damage that occurs in terms of the number of permanently displaced atoms per α -decay. These “active” experiments test the feasibility of the rigorous quantification of radiation damage/resistance in ceramics that are candidates for radionuclide immobilization.

The key safety consideration in an experiment with a radioactive sample is to prevent contamination or harmful exposures of the operator or equipment. This is accomplished by preparing the sample in a non-dispersible form. We used a diamond-tipped core drill to extract a 3-mm-diameter core from a sintered disk of a zircon-based ceramic. These cores were inserted into a ceramic holder to a maximum stacked height of 10 mm. This holder was sealed in a polytetrafluoroethylene capsule, and the whole assembly was loaded into a 7.5 mm zirconia rotor to form a triply contained sample (Figure 1). At each stage of



Figure 1. Exploded view of the triple-containment MAS rotor for radioactive samples. The innermost capsule in this depiction is made from a boron nitride ceramic; current designs use an aluminum nitride ceramic.

loading, the assembly is checked for external contamination. The rotor was then test spun and re-checked for contamination, and once cleared it was moved to the spectrometer. In proof-of-principle tests, we cored two ceramic samples that were prepared in 1984 with 10 wt% ^{239}Pu and ^{238}Pu loadings, respectively. For increased sensitivity the ^{29}Si MAS NMR signals were acquired with Carr, Purcell, Meiboom, and Gill (CPMG) echo trains.

^{239}Pu has a half-life of 24,100 years and ^{238}Pu a half-life of 87 years, thus the ^{238}Pu sample has received on the order of 10^{20} α -decays/g and the ^{239}Pu sample $\sim 5 \times 10^{17}$ α -decays/g. Figure 2 shows the spectra of the summed CPMG echoes. The ^{239}Pu sample shows very little damage, a result that agrees with data on naturally occurring ZrSiO_4 . This is an important result in terms of interpreting dose rate effects on radiation damage because this sample has received in 20 years the same dose a natural sample would have received in ~ 500 million years. The ^{238}Pu sample, on the other hand, has become completely amorphous due to its large α -dose, with some re-crystallization of an as yet unidentified phase. The stage is set to produce selected samples of ^{238}Pu -doped ceramics and quantitatively evaluate their radiation resistance with NMR spectroscopy.

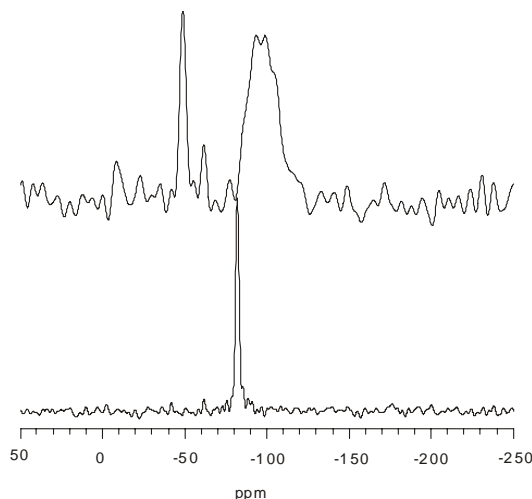


Figure 2. ^{29}Si MAS NMR spectra (sample spinning speed = 3.5 kHz) of a sintered zircon ceramic containing approximately 10 wt% ^{238}Pu (top) and ^{239}Pu (bottom). The spectra were acquired with a CPMG echo train. Sample masses were 75 mg and 52 mg for the ^{239}Pu and ^{238}Pu samples, respectively. The top spectrum reveals the highly amorphous state of the ^{238}Pu ceramic, which has received an internal α -dose more than two orders of magnitude higher than the ^{239}Pu specimen.

Reference

Farnan I and EKH Salje. 2001. "The Degree and Nature of Radiation Damage in Zircon Observed by Si-29 Nuclear Magnetic Resonance." *Journal of Applied Physics* 89:2084-2090.

Chemical Signatures in Thermal Springs: Atomic-Level Structure of Silicon and Aluminum in Natural and Synthetic Minerals

N Hinman,^(a) A Tenesch,^(a) and S Burton^(b)

(a) University of Montana, Missoula, Montana

(b) W.R. Wiley Environmental Molecular Sciences Laboratory, Richland, Washington

Many factors drive chemical change in geothermal systems. Long-term effects include climatic change; change in the location, quantity, and rate of release of heat; and volcanic processes. For example, climatic processes affect the amount of water circulating through the system and, therefore, the amount of heat released as steam and liquid water. Mid-term effects include seasonal processes and human impacts; for example, interactions between shallow groundwater and deeper thermal water can affect chemistry of the water in surface springs. Short-term effects include photochemical and photosynthetic processes; for example, reduced forms of iron are detected in mid-day because of photochemical processes whereas the by-products of such reactions apparently reduce sulfide concentrations. These changes result from changes in pH, redox conditions, and solution composition, and can impart chemical signatures in deposits formed in such springs.

What signatures are likely to be preserved in the geological record? Because chemical changes can affect the pH and redox conditions of thermal springs, it makes sense to pursue signatures of elements affected by these factors. Although many minor elements are affected by these changes, in this study we focus on changes in major element speciation.

In this study, we focus on changes in the concentrations and forms of aluminum and silicon in thermal springs of different compositions. Waters from an unnamed geyser in Shoshone Geyser Basin (Yellowstone National Park, Wyoming) and from the Trinoi Geyser (Krontoskii Reserve, Kamchatka, Russia) were selected to represent different spring water chemistries that might result from changes over a long time period or that might result from original differences in host rock composition.

Nuclear magnetic resonance (NMR) spectra acquired from instruments at the W.R. Wiley Environmental Molecular Sciences Laboratory show differences in the atomic environment of aluminum between waters from the unnamed U.S. geyser and the Trinoi Geyser (Figure 1). Water from the Trinoi Geyser shows significant quantities of both tetrahedrally coordinated aluminum and octahedrally coordinated aluminum. Water from the unnamed U.S. geyser has no octahedrally coordinated aluminum. The differences in the silicon environment in waters from the Trinoi and Pork Chop geysers are not as pronounced. Solid-state Si-NMR shows two distinct silicon environments. Results from cross-polarization experiments (Figure 2) show silicon bridging to two other silicon atoms via oxygen (Q2) and to three other silicon atoms via oxygen (Q3). Sinters from both Yellowstone National Park and the Krontoskii Reserve are a mix of these two silicon types.

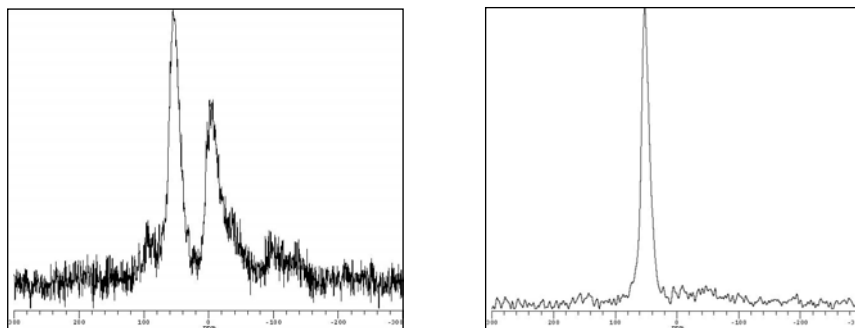


Figure 1. (Left): Aluminum NMR MAS spectra for siliceous sinter from the Kamchatka Peninsula. Significant quantities of both tetrahedral and octahedral aluminum are present. (Right): Aluminum NMR MAS spectra for siliceous sinter from Yellowstone National Park. This ^{27}Al spectrum shows only the tetrahedral aluminum species present.

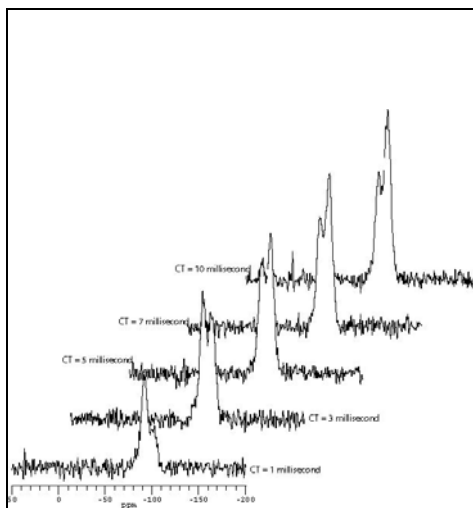


Figure 2. Cross-polarization (CP) MAS Si NMR spectra for siliceous sinter from the Kamchatka Peninsula. The array illustrates the affect of increasing CP contact times on the observation of Q2 and Q3.

Such differences in the aluminum's atomic environment may be attributed to effects of solution chemistry on the speciation of dissolved forms of aluminum. Speciation affects the rate and properties of solid deposition and, therefore, is the likely explanation in the observed differences in NMR spectra. Spring-water chemistry, therefore, affects the properties of solids formed there and may yield evidence of past changes.

Probing the Function of the Hypothetical Nudix Hydrolyase DR0079 from *Deinococcus radiodurans*

GW Buchko,^(a) S Ni,^(a) SR Holbrook,^(b) and MA Kennedy^(a)

(a) Pacific Northwest National Laboratory, Richland, Washington

(b) Lawrence Berkeley National Laboratory, Berkeley, California

It has been suggested that the radiation resistance of *Deinococcus radiodurans* is due to unusually efficient DNA repair mechanisms. One method for effecting proficient repair may be a DNA topology unique to *D. radiodurans* that makes it easier for DNA repair proteins to recognize and repair damage. Another source of the efficient repair may be a suite of redundant DNA repair proteins. Analysis of the complete genome sequence of *D. radiodurans* reveals an uncommonly high number of genes with potential DNA repair activities, essentially all of which have functional homologues in other procaryotes. Especially redundant are the 23 genes that have sequence homology with the Nudix family of polyphosphate pyrophospho-hydrolases. To better understand the relevance, function, and mechanism of the Nudix family of proteins and the roles played by the hypothetical *D. radiodurans* Nudix proteins in radiation resistance, we determined the solution structure of the hypothetical *D. radiodurans* Nudix protein DR0079 (171 residues, 19.3 kDa) using nuclear magnetic resonance (NMR)-based methods that included residual dipolar coupling (RDC) restraints (Buchko et al. 2003; Holbrook et al. 2003). A ribbon representation of the solution structure of DR0079 is shown in Figure 1.

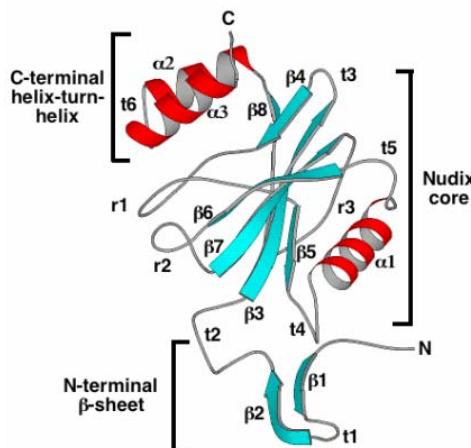


Figure 1. Ribbon representation of the solution structure of DR0079 (1Q27).

The protein contains eight β -strands and three α -helices organized into three subdomains: an N-terminal β -sheet (1 to 34), a central Nudix core (35 to 140), and a C-terminal helix-turn-helix (141 to 171). The Nudix core and C-terminal helix-turn-helix form the fundamental fold common to the Nudix family, a large mixed β -sheet sandwiched between α -helices. The residues that compose the signature Nudix sequence, the Nudix box, are contained in a turn-helix-turn motif on the face of the mixed β -sheet.

DR0079 has no identified biochemical function. Potential substrates and metal ligands for DR0079 were tested by chemical shift mapping, which is based on the premise that protein-ligand interactions usually perturb the chemical environment of the nuclei at the interface of ligand binding. Such perturbations are often accompanied by changes in the chemical shifts of the backbone $^1\text{H}^{\text{N}}$ and ^{15}N resonances. By identifying resonances that undergo a binding-dependent chemical shift or intensity perturbation, it is possible to identify ligands that bind to a protein and to map the location of the ligand binding site onto the three-dimensional structure of the protein. As shown in Figure 2, such experiments showed

DR0079 bound to the divalent cation Mg^{2+} . Similar experiments showed that DR0079 did not bind Mn^{2+} . Other chemical shift mapping experiments with potential substrates showed that DR0079 did not bind α,β -methyleneadenosine 5'-triphosphate (AMPCPP) or guanosine 5'-[β,γ -imido]triphosphate (GMPPNP), non-hydrolyzable substrate analogues for ATP and GTP, respectively.

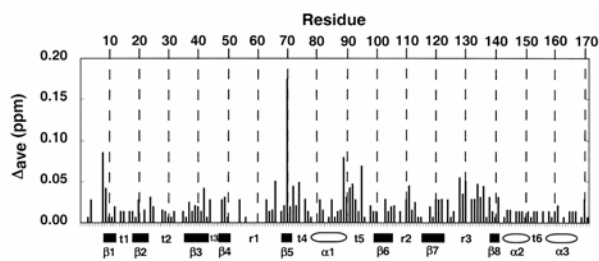


Figure 2. Combined average chemical perturbations in the 1H and ^{15}N resonances of DR0079 upon the addition of 100 fold excess $MgCl_2$.

These chemical shift mapping studies and other biochemical data suggest that DR0079, along with most of the other 22 hypothetical Nudix hydrolases, is not a nucleotide triphosphatase. Furthermore, global analysis of the *D. radiodurans* proteome using high-resolution mass spectroscopy methods show that DR0079 and the other 22 hypothetical Nudix proteins are predominately expressed in unstressed cells. If DR0079 and the other hypothetical Nudix hydrolases are not involved in DNA repair, then what role, if any, do they play in radiation resistance and desiccation protection? A possible answer to this question is that the *D. radiodurans* suite of Nudix hydrolases may be responsible for maintaining the physiological balance in the cell during the hours of chromosomal repair immediately following exposure to ionizing radiation or stress. Their function would be to remove potentially toxic, deleterious compounds that contain at least one diphosphate linkage from the cell. Such compounds include ADP-ribose, coenzymes, regulators, cell-signaling molecules, and intermediates in cellular metabolism (e.g., sugar nucleotides, NADH). Indeed, the only other known *D. radiodurans* Nudix structure, DR1184, turned out to be a “housecleaning,” functionally distinct Nudix hydrolase. Therefore, it is likely that DR0079 is also a “housecleaning” Nudix hydrolase with a functionally distinct purpose.

References

- Buchko GW, S Ni, SR Holbrook, and MA Kennedy. 2003. “ 1H , ^{13}C , and ^{15}N NMR Assignments of the Hypothetical Nudix Protein DR0079 from the Extremely Radiation-Resistant Bacterium *Deinococcus radiodurans*.” *Journal of Biomolecular NMR* 25:169-170.
- Holbrook EL, U Schulze-Gahmen, GW Buchko, S Ni, MA Kennedy, and SA Holbrook. 2003. “Purification, Crystallization, and Preliminary X-Ray Analysis of Two Nudix Hydrolases from *Deinococcus radiodurans*.” *Acta Crystallographica* D59:737-740.

Multinuclear Investigations of the Interactions between Glass and Crystalline Phases of Si, Li, Na, K, or Cl in Ceramic Waste Forms

MJ Lambregts,^(a) SM Frank,^(a) SD Burton^(b)

(a) Argonne National Laboratory West, Idaho Falls, Idaho

(b) W.R. Wiley Environmental Molecular Sciences Laboratory, Richland, Washington

Argonne National Laboratory, as part of the Spent Fuel Demonstration Project for the U.S. Department of Energy, has developed a glass-bonded sodalite ceramic waste form. This material immobilizes the fission-product and transuranic actinide-containing salt from the electrometallurgical treatment of spent sodium-bonded nuclear fuel into a stable product suitable for storage in a geological repository. Two of the standards for acceptance of waste into a geological repository are 1) the concentration of lithium and sodium that leaches from the waste form during product consistency tests must be less than that of the benchmark glass and 2) the chemical composition and crystalline phases of elements that compose more than 0.5 wt% of the waste form must be identified. The interactions displayed in these more simple systems are studied to obtain baseline information that can then be used to interpret the behavior of the more complex actual ceramic waste form.

In this project, interactions between the glass and crystalline phases of ceramic waste forms were investigated via powder x-ray diffraction, scanning electron microscopy, and ^{29}Si , ^{27}Al , ^{23}Na , ^7Li , and ^{35}Cl magic-angle-spinning nuclear magnetic resonance spectroscopy (MAS NMR). Some of the MAS NMR data was obtained at the W.R. Wiley Environmental Molecular Sciences Laboratory (EMSL) at Pacific Northwest National Laboratory. NMR chemical shifts are directly related to the shielding of the nucleus by the electronic structure of its immediate environment. Thus, they will be influenced by the identity and position of nearby atoms.

^{29}Si has a spin of $I = 1/2$ and is the only non-quadrupolar nuclei in the samples. Its spherical charge distribution makes spectral interpretation relatively simple. Figure 1 shows the ^{29}Si solid state MAS NMR spectra for all the samples. The important feature observed in the ^{29}Si spectra is the position of the peaks that indicate the various silicate structures with respect to silicon bonded to oxygen.

^{27}Al , ^{23}Na , ^7Li , and ^{35}Cl are all quadrupolar nuclei (^{27}Al $I = 5/2$; ^{23}Na , ^7Li , ^{35}Cl $I = 3/2$). The high natural abundance of these nuclei (75% or greater) and the fast relaxation times make these nuclei favorable to NMR spectroscopy, but the spectra of quadrupolar nuclei are complex if some site symmetry is not present. Nuclei with nuclear spins greater than $1/2$ have a nuclear quadrupole moment that interacts with the electronic field gradients within the sample. This interaction causes line broadening, distortion of the peaks, and displacement of the resonance from isotropic chemical shift. The compounds under study exhibit some of these effects to a lesser or greater extent. These changes in peak shape can reveal relative information on site symmetry. Measurement of solid-state spectra for the quadrupolar nuclei at

three different field strengths allows calculation of the isotropic chemical shifts. Solid-state spectra of the quadrupole nuclei attained at EMSL were acquired on the Infinity-plus 400 MHz instrument. Figure 2 shows ^{23}Na spectra taken at 500 MHz.

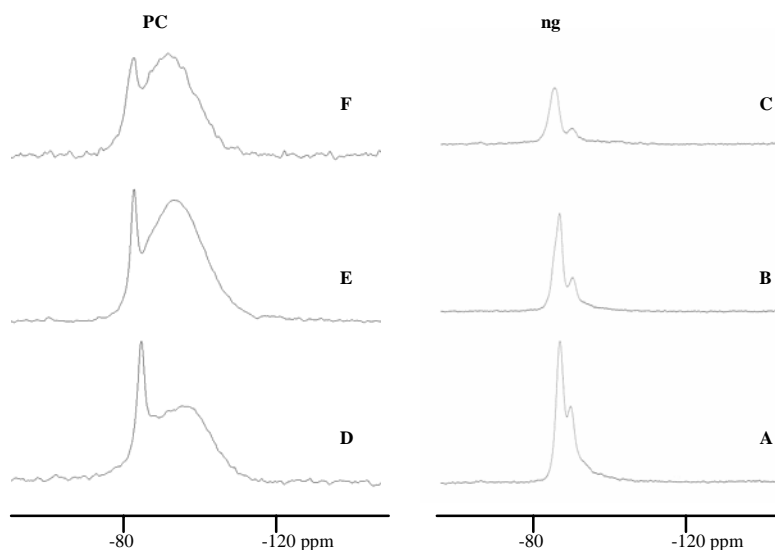


Figure 1. ^{29}Si NMR spectra: A. K-ng, B. Na-ng, C. Li-ng, D. K-PC, E. Na-PC, F. Li-PC. Spectra taken at 7.04 T.

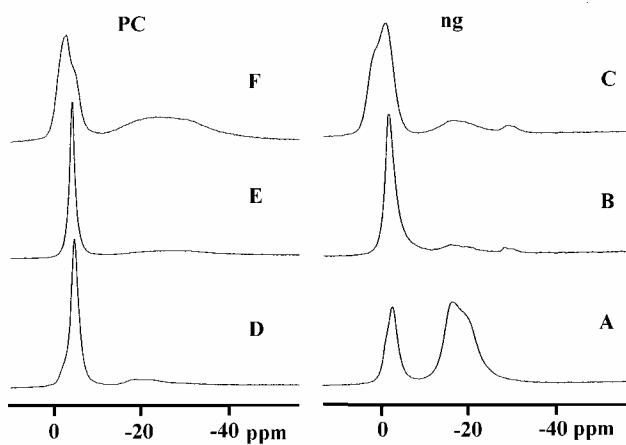


Figure 2. ^{23}Na NMR spectra: A. K-ng, B. Na-ng, C. Li-ng, D. K-PC, E. Na-PC, F. Li-PC. Spectra taken at 11.7 T. The narrow peaks are indicative of ^{23}Na situated in a relatively symmetric environment. The addition of potassium or lithium changes the line width and symmetry of the spectra features.

NMR Microscopy of Diffusive Transport in Natural Porous Mineral Grains

PD Majors^(a) and C Liu^(a)

(a) Pacific Northwest National Laboratory, Richland, Washington

Preliminary high-magnetic field ^1H nuclear magnetic resonance (NMR) microscopy (MRM) experiments were performed on water-saturated pristine mineral granules obtained from the vadose zone sediments at the U.S. Department of Energy's Hanford Site. A nearby uranium plume exists in the same sediment type, where uranium was found to be primarily associated within the grain microfractures. The transport behavior of the sediment-associated uranium is currently under investigation at the site. This study focuses on the fundamental properties of solute transport within the particle grains. Measurements included NMR imaging to assess the magnetic properties of several natural materials, and NMR relaxation and diffusion measurements in clean feldspar granules to characterize transport within pore spaces.

The granules were saturated with distilled water and measured via ^1H MRM (500-MHz Varian WB500) inside 4-mm OD tubes using a homebuilt MRM magnet insert. Initial testing of several particles for their magnetic properties showed that clean feldspar particles (those not containing dark inclusions) had acceptable properties for further NMR measurements. Ferromagnetic basalt particles induced severe shifting of the water signal in and around the particle and were deemed unusable for further studies. "Pure" quartz granules showed only minor water-signal distortions but no observable porosity (either optically or by NMR). A few weathered feldspar granules with low carbonate deposits were selected via optical microscopy. Microscopic imaging of some water-saturated granules showed evidence of weathering cracks close to the particle surface (Figure 1).

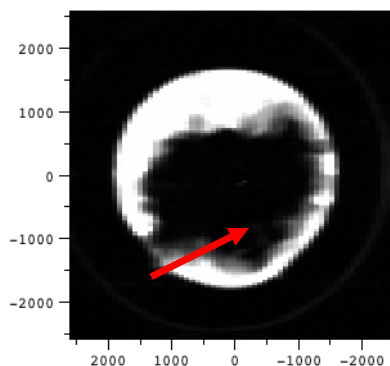


Figure 1. 500-MHz ^1H 2DFT MRM image for a magnetically clean feldspar granule (dark region) inside of a 4-mm OD NMR tube filled with distilled water (bright circle) with an arrow indicating the location of a possible weathering fracture.

Transport Measurements

The water-saturated granules were subsequently immersed in a ^1H -NMR-invisible perfluorinated oil, thereby restricting the water to individual particles and minimizing water signal external to the granules. NMR T_1 relaxation measurements (Figure 2) indicate the presence of two, essentially non-exchanging water compartments—one representative of bulk water and another representative of restricted water ($T_1=0.06$ and 3.16 sec) of approximately equal volume. These two compartments are assumed to correspond with surface-associated and bulk water, respectively. (Water in proximity to a mineral or biological surface is known to experience reduced NMR relaxation times.)

Subsequent bulk diffusion measurements for the restricted component were performed employing a diffusion sequence that was insensitive to the background gradient (Cotts et al. 1989). Several datasets were collected with differing diffusion times, and their resulting apparent diffusion rates were plotted in Figure 3 to yield the diffusion-time-dependent diffusion rate for granular water. Also shown in Figure 3 is the diffusion rate dependence for bulk water (not measured here). The range of diffusion intervals corresponds to a mean free diffusion distance of 3 to 50 microns for free water. Diffusion of the surface-associated water appears to be hindered at short diffusion times.

Further experiments are planned to measure diffusive transport over short and long time intervals in individual granules and packs. This information will be employed to characterize intra- and inter-granular transport processes. The feasibility of mapping directional diffusion (tensors) in individual granules will also be explored.

Reference

Cotts RM, MJR Hoch, T Sun, and JT Markert. 1989. "Pulsed Field Gradient Stimulated Echo Methods for Improved NMR Diffusion Measurements in Heterogeneous Systems." *Journal of Magnetic Resonance* 83:252-266.

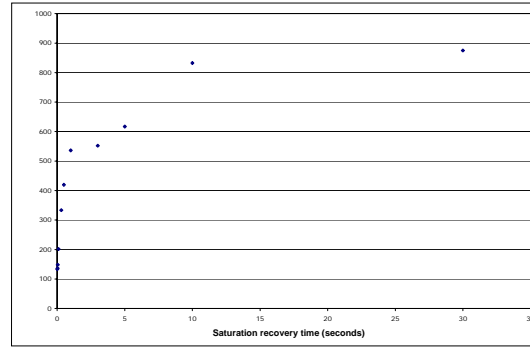


Figure 2. Spin-lattice (T_1) saturation recovery curve for a sample containing two feldspar particles saturated in water and immersed in a ^1H -NMR-invisible perfluorinated oil, thereby trapping the water near the particles to exclude interparticle water exchange. The particles were chosen via optical microscopy for low carbonate deposit content.

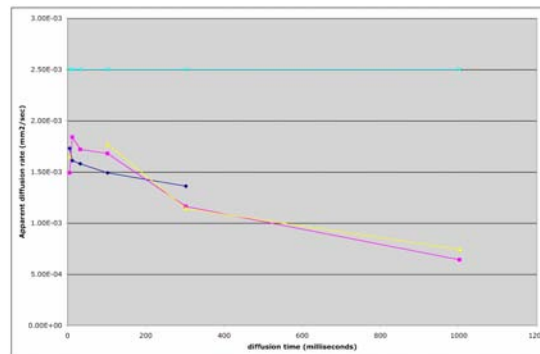


Figure 3. T_1 -filtered apparent diffusion rate as a function of diffusion interval for two feldspar particles immersed in fluorinated oil, and the theoretical diffusion rate for free water (top curve).

Compensating Bends in a 16-Base-Pair DNA Oligomer Containing a T₃A₃ Segment: An NMR Study of Global DNA Curvature

*K McAteer,^(a) R Michalczyk,^(b) A Aceves-Gaona,^(a) GW Buchko,^(c) NG Isern,^(d)
LA Silks,^(b) JH Miller,^(a) and MA Kennedy^(c)*

(a) Washington State University Tri-Cities, Richland, Washington

(b) Los Alamos National Laboratory, Los Alamos, New Mexico

(c) Pacific Northwest National Laboratory, Richland, Washington

(d) W.R. Wiley Environmental Molecular Sciences Laboratory, Richland, Washington

The origin of DNA curvature has been studied extensively, both experimentally and theoretically; however, a complete understanding has not yet emerged. It has been known for some time that A_nT_n segments when ligated in phase accumulate global curvature, while T_nA_n segments when ligated in phase do not, implying the importance of sequence context in DNA structure. Nuclear magnetic resonance (NMR) spectroscopy has been used to characterize the structure of A_nT_n- and T_nA_n-containing DNA segments in solution, but in the past, the accuracy and precision of those structures has been limited because of the inability of NMR to measure long-range nuclear Overhauser enhancements (NOEs) in DNA oligomers. With the introduction of residual dipolar coupling (RDC) restraints in NMR structure determination of proteins and nucleic acids, it has become possible to study long-range structural features in DNA, such as bending and curvature, with accuracy and precision that was unobtainable in the past. In addition, we have shown that inclusion of RDC restraints in restrained molecular dynamics calculations is essential to overcome the influence of the force field that can lead to inaccurate local structures in DNA oligomers (McAteer and Kennedy 2003); however, to date only a small number of DNA structures have been experimentally determined using RDC restraints.

In this paper, we discuss a high-resolution, solution-state structure of the 16-base-pair, self-complementary DNA oligomer [d(CGAGGT[†]TAAACCTCG)₂] containing a T_nA_n segment centered about a TpA step. The structure was refined with distance, torsion angle, and RDC restraints. We previously reported the NMR-derived solution structure of this oligomer refined only with distance restraints. Analysis of this structure indicated that poor base stacking at the TpA step may cause unusual base dynamics observed at the TpA step. Our current interest in this oligomer is threefold: 1) to determine if the degree and nature of bending observed in the high-resolution, RDC-refined structure can explain why simply reversing A_nT_n to T_nA_n abolishes anomalous polyacrylamide gel electrophoresis behavior; 2) to extend the application of RDC restraints to longer DNA sequences, thus allowing a comparison between NOE-only and NOE with RDC-refined structures and, consequently, enabling an assessment of the relative impact of RDC restraints and the force field on the final structure; and 3) to gain a better understanding of the structural origin of the large amplitude and slow base dynamics observed at TpA steps, sites in DNA where a significant variety of protein interactions and chemical reactions are localized.

RDC data was collected on the 500-MHz and 600-MHz NMR spectrometers at the W.R. Wiley Environmental Molecular Sciences Laboratory. Figure 1(A) shows part of the H6/H8 region of the ^1H - ^{13}C CT-HSQC-TROSY spectrum recorded for Base protons in the sample $[\text{d}(\text{CGAGGTTTAAACCTCG})_2]$ with ^{15}N , ^{13}C uniformly labeled residues in bold. The upper right TROSY components are shown in blue and the lower right components are shown in red. All C6-H6 couplings in the control sample were approximately 177 Hz. This spectral region is also shown in Figure 1(B) for the same sample aligned with ~ 25 mg/mL of Pf1 bacteriophage. The couplings increased to 221 Hz for T8 and T14 but were larger for T6 (236 Hz) and T12 (228 Hz). The upper right component (blue) and lower right component (red) of the ^1H - ^{15}N HSQC-TROSY spectra recorded in the control and in the aligned state for the same sample are shown in Figures 1(C) and (D), respectively. The magnitude of the RDC varies from ~ 18 Hz for T8 N3-H3 to ~ 23 Hz for T6 N3-H3.

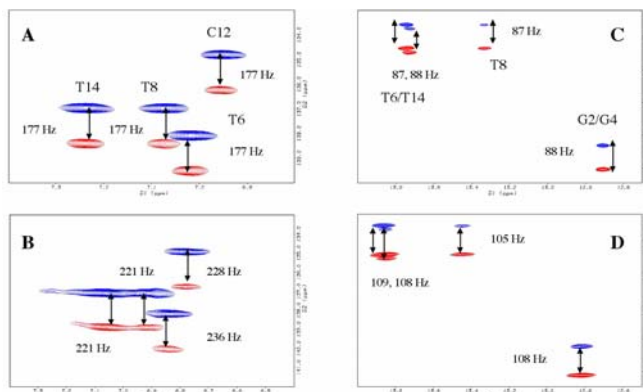


Figure 1. C6-H6 region of the ^1H - ^{13}C CT-HSQC-TROSY spectrum recorded for base protons in (A) the control sample $[\text{d}(\text{CGAGGTTTAAACCTCG})_2]$, and (B) the same sample aligned with ~ 25 mg mL $^{-1}$ Pf1 bacteriophage. ^{15}N - ^1H CT-HSQC-TROSY spectrum recorded for imino protons in the control sample (C), and the same sample aligned with ~ 25 mg/mL Pf1 bacteriophage (D).

Figure 2 illustrates the improvement in convergence when RDC restraints are used in NMR-based restrained molecular dynamics calculations of DNA. The 15 lowest energy structures calculated with NOE and torsion angle restraints only are shown on the left (root-mean-square deviation [RMSD] = 1.47 Å) and the 15 lowest energy structures calculated with the additional RDC restraints are shown on the right (RMSD = 1.03 Å). We are currently using these high-resolution structures to study adenine-induced curvature in DNA.

Reference

McAteer K and MA Kennedy. 2003. "Force Field Dependence of NMR-Based, Restrained Molecular Dynamics Calculations Including an Analysis of the Influence of Residual Dipolar Coupling Restraints." *Journal of Biomolecular Structure and Dynamics* 20:487-506.

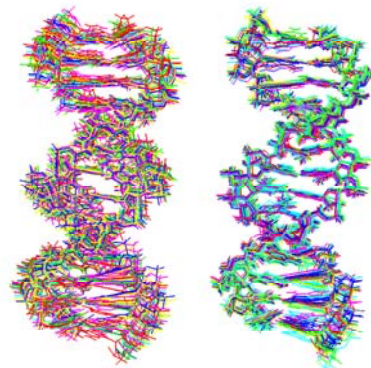


Figure 2. Superimposition of the 15 lowest energy structures calculated in the absence (left) and the presence (right) of RDC restraints in the restrained molecular dynamics calculations.

Metal-Binding Sites on Rhamnolipid Produced by *Pseudomonas aeruginosa*

W Otto,^(a) C Larive,^(b) and S Burton^(c)

(a) University of Maine at Machias, Machias, Maine

(b) University of Kansas, Lawrence, Kansas

(c) W.R. Wiley Environmental Molecular Sciences Laboratory, Richland, Washington

Because of their strong binding affinity for heavy metals, rhamnolipids are beginning to be used for remediation of metal-contaminated soils. To understand the differences in metal binding between different rhamnolipids, characterization of the metal-binding site on the rhamnolipid is important. The binding site for ^{113}Cd was probed using cross-polarization, magic-angle-spinning (CP MAS) ^{113}Cd nuclear magnetic resonance (NMR) and for Pb using MAS ^{207}Pb NMR. Further characterization of the metal-binding site was performed using CP MAS ^{13}C NMR on a pure rhamnolipid sample and a sample with added Cu. The paramagnetic Cu attenuates the resonance intensity of the ^{13}C atoms near the binding site. The NMR experiments conducted on the 300-MHz instrument at the W.R. Wiley Environmental Molecular Sciences Laboratory helped determine the binding site of metals to this rhamnolipid.

Figure 1, the ^{113}Cd NMR spectrum of the Cd(II)-rhamnolipid sample, shows one resonance indicating there is a single binding site. The broad line width indicates that there is significant mobility of the Cd nucleus. The chemical shift observed from this spectrum is similar to that of acetate and, hence, is consistent with the Cd(II) binding through two carboxylate functionalities and perhaps other oxygen-containing functionalities. This result would be consistent with prior reports that the stoichiometry of metal binding is 2 rhamnolipid to 1 Cd.

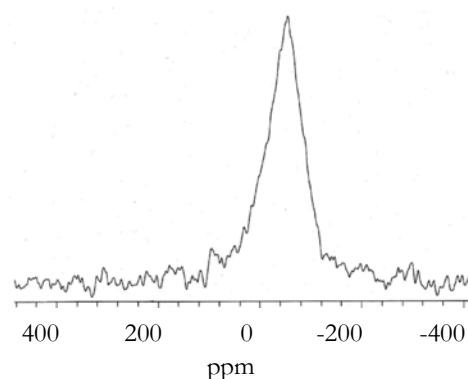


Figure 1. ^{113}Cd CP MAS NMR spectrum of a Cd-rhamnolipid sample.

Figure 2 illustrates the attenuation that arises from the presence of paramagnetic copper. The resonances of the rhamnolipid sample with copper (top) are broader than those of the rhamnolipid without copper (bottom). In these spectra, several resonances that are almost completely attenuated are observed, indicating the carbon atoms of the binding sites. The ^{13}C resonances have been assigned previously (Moon et al. 1996). Based on the assigned resonances, the binding site can be more completely described. The attenuation of the resonance near 180 ppm, that of the carbon in the carboxylate endgroup, as well as the resonance near 90 ppm, the 1' carbon on the rhamnose head (see Figure 3) attached through the ether connection to the backbone of the rhamnolipid, indicate that these two carbon atoms are part of the metal-binding site. The resonance at 40 ppm and to some extent the resonance at 70 ppm, corresponding to the carbons between the ether and ester linkages in

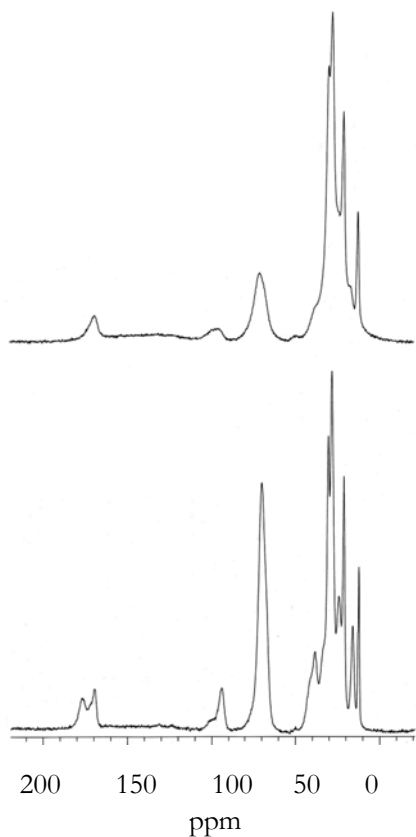


Figure 2. Top: ^{13}C MAS NMR of rhamnolipid with 5% copper loading. Bottom: ^{13}C MAS NMR of rhamnolipid.

the backbone are also attenuated, indicating they are part of the binding site. This is the first evidence that the sugar and to some extent the ether linkage are involved in metal binding.

These results imply that solid-state NMR techniques could be applied to the observation of other classes of rhamnolipids such as di-rhamnolipids. Changes in metal bonding to the chelate due to size and flexibility may be investigated by these techniques.

An attempt was made to measure the ^{207}Pb MAS NMR spectrum of the rhamnolipid complex; however, artifacts in the spectrum preclude the gleaning of any valuable information.

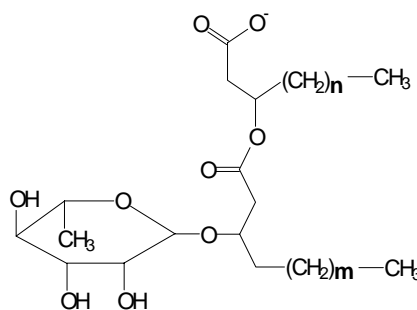


Figure 3. Structure of the rhamnolipid studied in this project.

Reference

Moon S, P Kang, B Kim, and B Hwang. 1996. "Spectral Evidence of 1,2-Linkage in Antifungal Rhamnolipid Produced by *Pseudomonas aeruginosa*." *Bulletin of the Korean Chemical Society* 17:291-293.

Mammalian Chromatin High-Mobility Group Protein HMGA1: NMR Evidence for a Complex with a 32-Residue Double-Stranded DNA Oligomer

GW Buchko,^(a) R Reeves,^(b) MJ Smerdon,^(b) and MA Kennedy^(a)

(a) Pacific Northwest National Laboratory, Richland, Washington

(b) Washington State University, Pullman, Washington

Chromatin high-mobility group protein (HMGA1) belongs to a family of nonhistone mammalian proteins that are thought to be important structural components affecting the conformation and function of chromatin. These proteins are also known as architectural transcription factors because of their ability to function as components of chromatin structure and as auxiliary gene transcription factors (Reeves 2001). Over-expression of HMGA1 has been observed in different types of human cancers, and it has been demonstrated that such over-expression inhibits the transcription of gene coding for several proteins involved in DNA repair, including DNA ligase III, Dnase X, ATM, and DNA methyltransferase. Thus, HMGA1 is also an oncoprotein. HMGA1 binds DNA preferentially to the narrow minor groove of A•T-rich segments. Studies suggest that it is the structure of the A•T-rich DNA that HMGA1 recognizes rather than the sequence. A•T-rich DNA is a potential target for the major type of damage exposure to ultraviolet radiation, cyclobutane pyrimidine dimers (CPD), lesions that bend and unwind DNA. Consequently, there are a number of scenarios as to how HMGA1 and CPD lesions interact in the nucleus. HMGA1 binding to A•T-rich DNA may protect it from ultraviolet damage. HMGA1 may recognize CPD lesions in A•T-rich DNA and either facilitate, or prevent, DNA repair. CPD lesions may act to prevent the binding of HMGA1 to A•T-rich DNA or displace them from the region once formed. To date, the experimental evidence does not exclusively favor any one of these scenarios and experiments are in progress to establish which of these scenarios are most likely.

Human HMGA1 is a relatively small protein of 107 amino acid residues with a molecular weight of 11.9 kDa. The protein has been purified, expressed, and isotopically labeled using bacterial expression systems. Many studies show that HMGA1 only adopts a structure when bound to A•T-rich DNA. It binds DNA via structural motifs called “A•T hooks.” As shown in Figure 1, HMGA1 contains three A•T hooks labeled DBD-1, DBD-2, and DBD-3. An NMR structure has been determined for a truncated version of HMGA1, residues 50 to 91, (containing DBD-2 and DBD-3) bound to two DNA dodecamers (Huth et al. 1997). The structure shows that both A•T hooks bind DNA in the minor groove of A•T-rich regions. While this structure provides valuable insights into how HMGA1 interacts with A•T-rich DNA, the structure of A•T-rich DNA may be radically different when all three A•T hooks on one molecule of HMGA1 wrap around one molecule of A•T-rich DNA.

```
MSESSSKSSQPLASKQEKDGTTEKRGRGRPRKQPPVSPGTALVGSQKEPSEVP 52
                                DBD-1
TPKRPRGRPKGSKNKGAATRKTTTTPGRKPRGRPKKLEKEEEEISQESSEEEQ 107
    DBD-2                                DBD-3
```

Figure 1. Organization of human HMGA1 showing in red the position of the three DNA binding domains, DBD-1, DBD-2, and DBD-3.

Each of the three A•T hooks in HMGA1 binds a 5 to 6 base-pair stretch of A•T-rich DNA. The tandem binding of all three A•T hooks suggests that an intact HMGA1 protein should be capable of associating with ~15 to 18 base pairs of contiguous A•T residues, a prediction verified by various protein-DNA footprinting methods. Fluorescence competition assays and preliminary electrophoretic mobility shift experiments have demonstrated that the synthetic double-stranded DNA 32-mer, d(GTCATC(A)₁₉CAGTTC) (A19), binds to all three A•T hooks of HMGA1. We have recently verified the formation of a HMGA1-A19 complex using nuclear magnetic resonance spectroscopy.

Figure 2 (left) shows the ¹H/¹⁵N HSQC spectrum of free, ¹⁵N-labelled HMGA1. The narrow dispersion of the amide cross peaks is characteristic of a protein lacking a well-defined secondary structure. Figure 2 (right) shows the ¹H/¹⁵N HSQC spectrum of HMGA1 in the presence of A19. While the dispersion of the amide cross peaks is still narrow, relative to free HMGA1 the line widths are broader, fewer cross peaks are observed, and the chemical shifts of most of the cross peaks that are observed have been significantly perturbed. These initial spectroscopic results suggest that a protein-DNA complex has formed and are an encouraging first step towards determining the solution structure of HMGA1 using all three of its A•T hooks to wrap around one molecule of A•T-rich DNA.

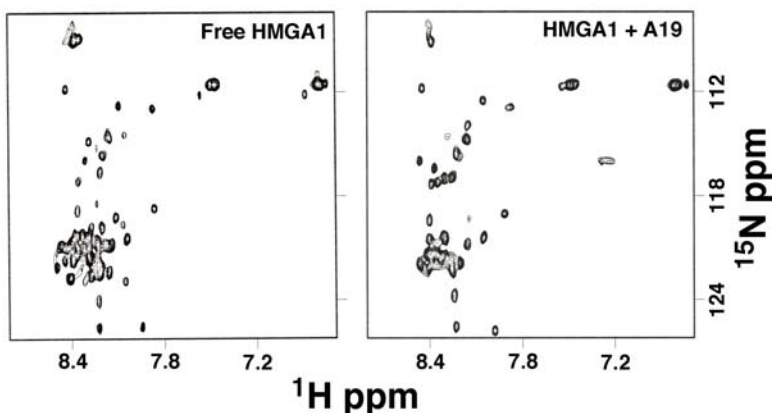


Figure 2. ¹H/¹⁵N HSQC spectrum of free HMGA (left), and in the presence of the 32-residue double-stranded DNA oligomer A19 (right). Spectra were recorded at a ¹H resonance frequency of 800 MHz, 25°C.

References

- Huth JR, CA Bewley, MS Nissen, JNS Evans, R Reeve, AM Gronenborn, and GM Clore. 1997. "The Solution Structure of an HMG-I(Y)-DNA Complex Defines a New Architectural Minor Groove Binding Motif." *Nature Structural Biology* 4:657-668.
- Reeves R. 2001. "Molecular Biology of HMGA Proteins: Hubs of Nuclear Function." *Gene* 277:63-81.

Structure Determination of Membrane Proteins

K Choowongkamon,^(a) CR Sanders,^(b) and FD Sönnichsen^(a)

(a) Case Western Reserve University, Cleveland, Ohio

(b) Vanderbilt University, Nashville, Tennessee

Although they account for about 30% of the genetically coded proteins in all organisms, membrane proteins (MPs) are structurally underdetermined and present only a small fraction of known structures to date. This is a consequence of the difficulty represented by their native membrane environment for the common techniques of protein structure determination. Nevertheless, significant progress has been made in recent years using x-ray crystallography and nuclear magnetic resonance (NMR) spectroscopy. In the latter, transverse-relaxation optimized spectroscopy-based experiments largely overcome the size limitations of NMR and, thus, have made the use of detergent micellar solutions of proteins practical. Prokaryotic diacylglycerolkinase

Prokaryotic diacylglycerolkinase (DAGK) is a homotrimeric integral membrane protein composed of 13 kDa subunits, with each subunit having three transmembrane helices. After successful determination of three outer-membrane, monomeric barrel MPs (Abildgaard et al. 2001; Fernandez et al. 2001; Hwang et al. 2002), DAGK represents the next step of difficulty for NMR structural determination, as it is largely a helical and larger-size molecule. DAGK-DPC mixed micelles are complexes of 96k Da size, and our studies have significantly benefited from access to ultra-high magnetic field strengths. Following the partial assignments of backbone resonances (Oxenoid et al. 2002), data recently acquired through use of the 800-MHz spectrometer at the W.R. Wiley Environmental Molecular Sciences Laboratory have included four-dimensional NMR experiments, which proved particularly helpful in completing and confirming the resonance assignments (Figure 1). These experiments facilitated the nearly complete resonance assignment of a polytopic MP (Oxenoid et al. 2002), thus removing the major obstacle for a structure determination by NMR. Juxta-Membrane Domain of the Epidermal Growth Factor Receptor

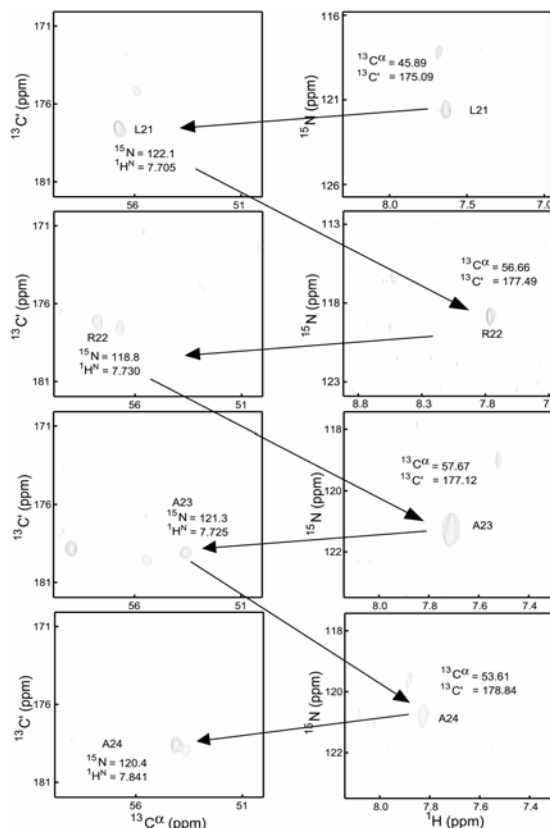


Figure 1. Example planes of the 4D-HNCOCA and HNCACO experiments of DAGK at 800 MHz.

The epidermal growth factor receptor (EGFR) is a member of a family of four receptors [EGFR (or ErbB1), ErbB2, ErbB3, and ErbB4] with intrinsic tyrosine kinase activity. It consists of a large extracellular domain, a single-helix transmembrane region, and a cytosolic kinase domain, and is widely expressed on many cell types, including epithelial and mesenchymal lineages. Upon activation by at least five distinct ligands, the intrinsic kinase is activated, and EGFR and numerous intermediary effector molecules are dimerized and phosphorylated. This initiates several signaling pathways that cause important biological responses, such as mitogenesis or apoptosis, enhanced cell motility, protein secretion, and differentiation or dedifferentiation. In addition to being implicated in organ morphogenesis, maintenance, and repair, unregulated EGFR signaling has been correlated with a wide variety of tumors with increased cell division, and other aspects of malignant tumor progression, such as angiogenesis, metastasis, and inhibition of apoptosis.

The activity of the EGFR receptor is tightly regulated by compartmentalization and ligand-induced endocytosis. Sorting signals—short, amino acid sequence motifs in the juxta-membrane domain of this receptor—are responsible for interaction of the receptor with a complex sorting machinery of the cell (i.e., the specific targeting and transport of the receptor to the baso-lateral cell membranes in polarized cells, and the rapid internalization, sorting, and degradation of activated receptor in lysosomes). Our studies have focused on the structural properties of the two baso-lateral and one endosome-to-lysosome sorting signals present in the juxta-membrane domain (Figure 2). We used the increased resolution and sensitivity of EMSL's 800-MHz NMR spectrometer to conduct a hetero-nuclear edited ^{13}C - and ^{15}N -edited nuclear overhauser enhancement spectroscopy experiment on DPC-micelle complexes of the EGFR-juxta-membrane domain. The objective of the experiment was to identify tertiary contacts between the sorting signals that may explain their interaction and regulation and the dominance of the baso-lateral signal in the resting receptor. Structural refinement using data from the experiment is nearing completion.

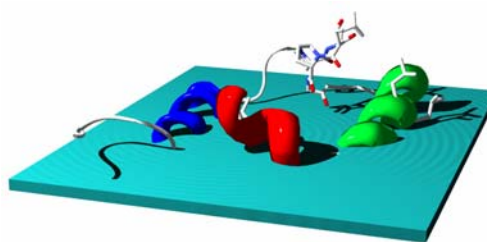


Figure 2. Preliminary structure of the EGFR juxta-membrane domain highlighting the nearly planar arrangement of three helices and the flexible region of the dominant baso-lateral sorting signal.

References

- Abildgaard AF, JH Bushweller, and LK Tamm. 2001. "Structure of Outer Membrane Protein A Transmembrane Domain by NMR Spectroscopy." *Natural Structural Biology* 8:334-338.
- Fernandez K, Adeishvili, and K Wuthrich. 2001. "Transverse Relaxation-Optimized NMR Spectroscopy with the Outer Membrane Protein OmpX in Dihexanoyl Phosphatidylcholine Micelles." *Proceedings of the National Academy of Sciences* 98:2358-2363.

Hwang PM, W-Y Choy, EI Lo, L Chen, JD Forman-Kay, CRH Raetz, GG Prive, RE Bishop, and LE Kay. 2002. "Solution Structure and Dynamics of the Outer Membrane Enzyme PagP by Nuclear Magnetic Resonance." *Proceedings of the National Academy of Sciences* 99:13560-13565.

Oxenoid K, FD Sönnichsen, and CR Sanders. 2002. "Topology and Secondary Structure of the N-Terminal Domain of Diacylglycerol Kinase." *Biochemistry* 41:12876-12882.

Structure of Human Telomerase

T Leeper,^(a) SL Reichow,^(a) KS Godin,^(a) and G Varani^(a)

(a) University of Washington, Seattle, Washington

Telomerase is the ribonucleoprotein (RNP) enzyme responsible in most eukaryotes for the replication of the chromosome termini (telomeres). It also plays a critical role in cellular division and cancer: it is activated in the germ line and in the great majority of cancer cells. It is composed of a 400-nucleotide ribonucleic acid (RNA) molecule and several proteins that associate with it, carry out the enzymatic activity, and promote its cellular localization and assembly. We are studying the structure of two critical domains of human telomerase RNA responsible for RNA biogenesis and for recruitment of the catalytic activity to the holoenzyme. Four proteins of unknown structure bind to human telomerase RNA: in doing so, they stabilize the RNA in the cell and direct its processing and nuclear localization. We aim to determine the structures of three such proteins (called Nop10, Nhp2, and Gar1) and of the RNA domains they associate with. Nuclear magnetic resonance (NMR) spectroscopy studies conducted at University of Washington and W.R. Wiley Environmental Molecular Sciences Laboratory (EMSL) have provided us with very high-quality data for all three proteins, for an RNA sub-domain (called CR7) that is essential for telomerase biogenesis, and for the entire domain of 80 nucleotides responsible for RNP assembly. Our goal is to dissect the structure and conformational flexibility of these domains and of the proteins that bind to them by combining well-established methods of NMR structure determination with new methods based on residual dipolar couplings. NMR experiments conducted at EMSL have already contributed significantly to our progress towards determining the structures of critical domains of human telomerase RNA and its associated proteins.

Structure of Telomerase Binding Proteins

Researchers are using very high quality NMR spectra (a nuclear Overhauser enhancement spectroscopy [NOESY] spectrum is shown in Figure 1) to determine the structure of the Gar1 protein. Its structure is unknown, but it has been proposed to be related to Sm proteins, a family of RNA-binding protein that form ring-like structures on U-rich RNAs and that associate with yeast telomerase RNA. Two additional proteins (γ Nop10 and γ Nhp2) are currently being investigated as well. NMR spectra collected at EMSL demonstrate that structure determination will be possible for at least Nop10, another protein of unknown structure but with critical functions in the biogenesis of telomerase and of the ribosome.

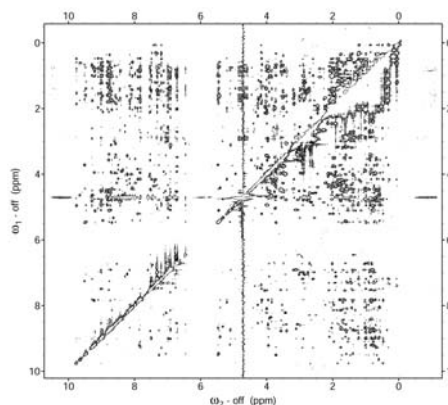


Figure 1. NOESY spectrum of archeal Gar1 protein, a key component of human telomerase.

The CR4/CR5 Domain of Human Telomerase

Human and mouse CR4/CR5 domains reconstitute telomerase activity when combined with the template domain and are, therefore, key functional elements of vertebrate telomerases. The NMR work on the CR4/CR5 domain conducted at EMSL has progressed to the point that we are now refining its structure by using new NMR methods based on residual dipolar couplings (a preliminary structure of the apical part of the domain is shown in Figure 2, together with the structure of another conserved stem-loop completed in 2003). The P6.1 stem-loop (Leeper et al. 2003) interacts with the template domain and promotes the tertiary folding of the RNA and perhaps even participates in catalysis. Completion of the structure will provide unprecedented insight into the structure/function of this key eukaryotic enzyme.

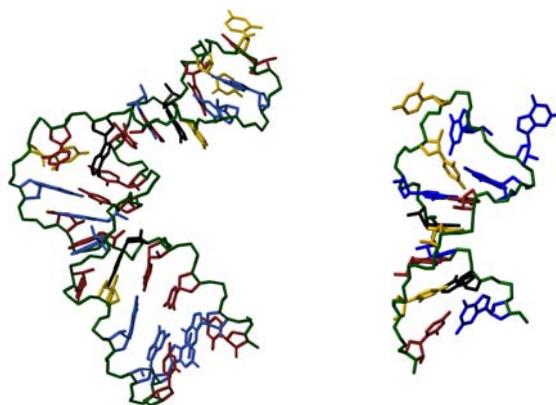


Figure 2. Structures of two key domains of human telomerase RNA responsible for activation of the enzymatic activity.

Reference

Leeper TL, N Leulliot, and G Varani. 2003. "The Solution Structure of an Essential Stem-Loop of Human Telomerase RNA." *Nucleic Acids Research* 31:2614-2621.

Structural Characterization of the *Escherichia coli* Mut M (Fpg) Protein: NMR Evidence for Conformational Changes upon DNA Binding

GW Buchko,^(a) K McAteer,^(b) SS Wallace,^(c) and MA Kennedy^(a)

(a) Pacific Northwest National Laboratory, Richland, Washington

(b) Washington State University Tri-Cities, Richland, Washington

(c) University of Vermont, Burlington, Vermont

Maintaining genomic integrity is critical to all living organisms, and cells have developed a number of repair mechanisms dedicated to genomic preservation. These mechanisms are necessary because DNA is a reactive molecule. In aqueous solution, DNA can react with many types of exogenous and endogenous agents that generate many types of DNA damage. Perhaps the most important agents are reactive oxygen species, such as hydrogen peroxide, superoxide radical anions, and hydroxyl radicals, because they are always present in cells as a consequence of normal cellular metabolism. Over 100 different DNA modifications have been identified because of the reaction of DNA with these endogenous reactive oxygen species. One of the most prominent lesions generated is 7,8-dihydro-8-oxoguanine (8-oxoG), a lesion implicated in mutagenesis, carcinogenesis, and ageing. While the number of chemically and physically distinct DNA lesions generated by reactive oxygen species is large, the DNA repair mechanism that repairs the majority of these nonbulky lesions, base excision repair (BER), is composed of a relatively small number of DNA glycosylases. In human cells approximately 10 DNA glycosylases involved in BER have been identified while eight have been found in the bacterium *Escherichia coli*.

Recently, a great deal of three-dimensional structural information has been obtained for free Fpg and Fpg in complex with DNA. However, to date, no crystal structure has been obtained for free and DNA-bound Fpg using an enzyme from the same bacteria. Hence, it has not been possible to determine unambiguously, from the crystal data, if any conformational changes are associated with DNA binding to Fpg. As shown in Figure 1, the N- and C-terminal domains of Fpg appear to “clamp” around the DNA. Solution studies indicate significant changes in the fluorescence of internal tryptophan residues in Fpg upon binding to DNA, suggesting that the conformation of the protein also changes significantly upon DNA binding. We have recently assigned much of the ¹H/¹⁵N HSQC NMR spectra of free Fpg (Buchko et al. 2002) and Fpg bound to a 13-residue, double-stranded DNA containing 1,3 propanediol (X), (13-PD), where X represents a non-hydrolyzable, abasic site analogue.

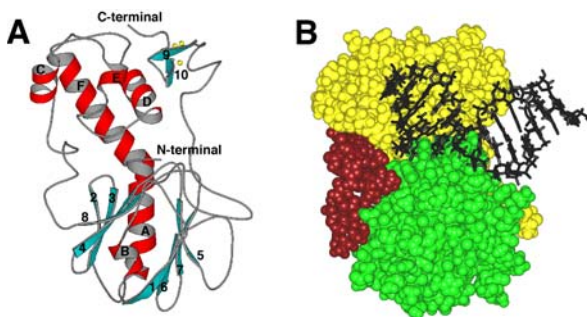


Figure 1. (A). Molscript ribbon representation of *E. coli* Fpg in the Fpg/DNA covalently cross-linked crystal structure (1K82). (B). CPK-space filled model of (A) with the N-terminal domain colored green, the C-terminal domain colored yellow, and the linker colored red. The covalently cross-linked DNA is represented by a black stick structure. The center residue in one strand of the DNA 13-mer is cross-linked to the protein at the N-terminal.

Figure 2 indicates that Fpg binds to the 13-PD tightly ($K_D > 10^{-6}$ M) because two peaks are observed for many resonances at Fpg:13-PD molar ratios that are less than 1:1 (e.g., V105). The Trp ring ϵ 1 proton was only observed for three of the five Trp residues in the $^1\text{H}/^{15}\text{N}$ HSQC spectrum. As illustrated in Figure 2, one of these residues, W35, is significantly

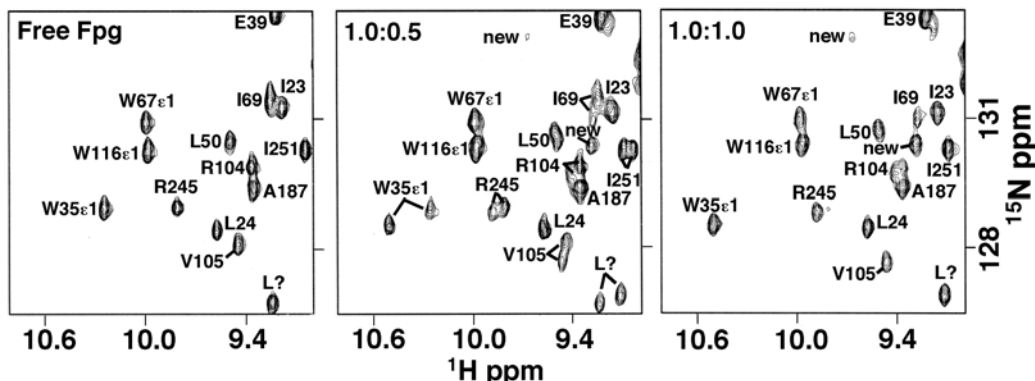


Figure 2. Portion of the $^{15}\text{N}/^1\text{H}$ HSQC spectrum of Fpg free in solution (left) and in the presence of approximately 0.5 (middle) and 1.0 molar (right) ratios of 13-PD. Spectra were recorded at a ^1H frequency of 900 MHz, 25°C. At Fpg:DNA molar ratios less than 1:1, two cross-peaks are observed for a subset of residues.

perturbed upon the addition of 13-PD. This residue was not observed to make contact with the DNA in the crystal structure; however, as shown in Figure 3, W35 is near the DNA binding pocket. Such a chemical shift perturbation to W35 is likely due to conformational changes to Fpg upon DNA binding and is consistent with the “freezing-out” of μsec to msec motion of the backbone amide residues of D91 and H92 (observed from CPMG NMR experiments) that was also observed when Fpg bound to 13-PD.

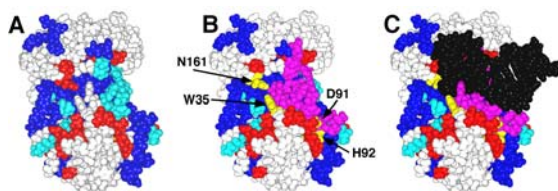


Figure 3. (A) CPK-space-filled model of Fpg from Figure 1. (B) W35, is shown in yellow as are the two residues, D91 and H92, whose motion is slowed down upon the addition of 13-PD (as suggested by CPMG experiments). The residues that make specific contact with the DNA, as observed in the crystal structure, are shown in purple. (C) The DNA in the Fpg/DNA covalent structure (1K82) is reintroduced onto the structure of Fpg as a CPK-space-filled model.

Reference

Buchko GW, SS Wallace, and MA Kennedy. 2002. “Base Excision Repair: NMR Backbone Assignments of *Escherichia Coli* Formamidopyrimidine-DNA Glycosylase.” *Journal of Biomolecular NMR* 22:301-302.

Structural Proteomics: Annotating the Genome Using Three-Dimensional Structure

A Yee,^(a) Bin Wu,^(a) TA Ramelot,^(b) JR Cort,^(b) MA Kennedy,^(b) and C Arrowsmith^(a)

(a) University of Toronto, Toronto, Canada

(b) Pacific Northwest National Laboratory, Richland, Washington

The three-dimensional structure of protein reveals several biochemical properties and functions that escape prediction based only on primary sequence. Structural proteomics is a genome-wide scale structural biology. Our ongoing structural proteomics project uses nuclear magnetic resonance (NMR) spectroscopy as one of the methods for obtaining the solution structure of proteins. Our laboratory at the University of Toronto screens and makes samples amenable for structure determination by NMR spectroscopy. We rely heavily on the advanced NMR capabilities at the W.R. Wiley Environmental Molecular Sciences Laboratory for collection of triple-resonance NMR experiments. The structures of a yeast protein and two ribosomal proteins from the archaea *Methanobacterium thermoautotrophicum* have recently been solved bringing the total to 14 structures solved so far in this collaboration.

Ribosomal Proteins S17E and S28E

Ribosomes are protein complexes required for protein synthesis in all organisms. S17E and S28E are two of the 28 proteins that make up the 30S ribosome in archaea. The S28E is an all- β strand protein while the S17E is an all- α helical protein (Wu et al. 2003).

Both proteins have very high sequence homology to their human ribosomal protein counterpart. The structure of these archaeal proteins provides a good template for modeling human proteins. Figure 1 shows the solution structures of S28E, S17E and YHR087W proteins as determined by NMR spectroscopy.

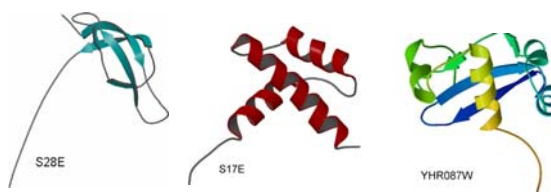


Figure 1. Solution structures of S28E, S17E, and YHR087W proteins as determined by NMR spectroscopy.

YHR087W

YHR087W is a protein from *Saccharomyces cerevisiae*, and it was annotated as a hypothetical protein because it has no sequence homologues to any protein of known function. Its three-dimensional structure revealed a resemblance to a domain of the Shwachman-Bodian-Diamond Syndrome protein, a human disease protein. Further structure comparison of the two proteins reveals common features that are likely to be functionally important. Further characterization based on this resemblance is ongoing.

Reference

Wu B, A Yee, A Pineda-Lucena, A Semesi, TA Ramelot, JR Cort, JW Jung, A Edwards, W Lee, M Kennedy, and CH Arrowsmith. 2003. "Solution Structure of Ribosomal Protein S28E from *Methanobacterium thermoautotrophicum*." *Protein Science* (12):2831-2837.

User Projects

Structural Studies of *Escherichia coli* Formamidopyrimidine DNA N-Glycosylase and Its Main Biological Substrate 8-Oxoguanine

SS Wallace

University of Vermont, Burlington, Vermont

Solid-State NMR Study of Molecularly Engineered Nano-Porous Materials

L Wang

Pacific Northwest National Laboratory, Richland, Washington

Nuclear Spin Relaxation Measurements for Structural Genomics

GT Montelione, RK Paranj

Rutgers University, Piscataway, New Jersey

AG Palmer

Columbia University, New York, New York

T Szyperski

State University of New York at Buffalo (SUNY), Buffalo, New York

Solid-State NMR Study of Conformation and Dynamics of Block Co-Polymer Composites

L Wang

Pacific Northwest National Laboratory, Richland, Washington

Analysis of High Surface Area Aluminas by ^1H and ^{27}Al NMR Methods

DA Lindquist, RM Hawk

University of Arkansas, Little Rock, Arkansas

Structural Biology of the Nudix Proteins from the Extremely Radiation-Resistant Bacterium *Deinococcus radiodurans*

GW Buchko, MA Kennedy

Pacific Northwest National Laboratory, Richland, Washington

SR Holbrook, DE Wemmer

Lawrence Berkeley National Laboratory, University of California, Berkeley, California

Molecular Probes of Quinol Oxidation by the Cytochrome b₆f Complex

DM Kramer, AG Roberts, IP Forquer, JL Cape

Washington State University, Pullman, Washington

ENDOR of Trityl Radicals

C Mailer

University of Chicago, Chicago, Illinois

Atomic-Level Structure of Silicon and Aluminum in Natural and Synthetic Minerals

NW Hinman

University of Montana, Missoula, Montana

NMR Studies on Nano-Materials*L Wang*

Pacific Northwest National Laboratory, Richland, Washington

Solid-State NMR Characterization of Synroc and Its Constituent Phases*JV Hanna*Australian Nuclear Science & Technology Organization (ANSTO), Menai
New South Wales, Australia**Ultra-High Field NMR Studies of Stable Isotope Applications***LA Silks*

Los Alamos National Laboratory, Los Alamos, New Mexico

Structural Proteomics of *Mycobacterium tuberculosis**TC Terwilliger*

Los Alamos National Laboratory, Los Alamos, New Mexico

NMR Structural Investigations of BRCA1*RE Klevit, PS Brzovic*

University of Washington, Seattle, Washington

Spatial Properties of Clustered Free Radicals Produced in DNA and Biosimulators by Ionizing Radiation*JD Zimbrick*

Purdue University, West Lafayette, Indiana

Solid-State ⁶⁷Zn NMR of Synthetic Metalloprotein Models*G Parkin*

Columbia University, New York, New York

Structural Determination of a Complex Membrane Protein, Diacylglycerol Kinase*CR Sanders*

Vanderbilt University, Nashville, Tennessee

FD Soennichsen

Case Western Reserve University, Cleveland, Ohio

Solid-State NMR Spectroscopy of Half-Integer Spin Quadrupolar Nuclei at High Magnetic Field Strengths: A Continuing Study of Model Boron and Molybdenum Compounds*RE Wasylshen, DL Bryce, MA Forgeron*

University of Alberta/Dalhousie University, Edmonton, Alberta, Canada

High-Field Solid-State ²⁵Mg NMR Studies of Inorganic and Biological Magnesium Compounds*KJ Ooms, RE Wasylshen*

University of Alberta/Dalhousie University, Edmonton, Alberta, Canada

Characterization of the Mineral Phases of Matrix Vesicles During Induction of Crystalline Mineral Formation*RE Wutbier*

University of South Carolina School of Medicine, Columbia, South Carolina

Zr-91 Nuclear Magnetic Resonance Studies of Solid Zirconium Compounds*RE Wasylshen, KW Feindel*

University of Alberta/Dalhousie University, Halifax, Nova Scotia, and British Columbia, Canada

Use of NMR Microscopy to Examine Biofilm Structure in Porous Media Under Conditions of Fluid Flow*BD Wood*

Oregon State University, Corvallis, Oregon

PD Majors, KR Minard

Pacific Northwest National Laboratory, Richland, Washington

NMR Studies of the Initial Reaction Products of Diacetylbenzene Isomers with Lysine and Proteins*PS Spencer, MI Sabari, M Kim*

Oregon Health Sciences University/Oregon Graduate Institute, Portland, Oregon

Separating the Lineshapes of the Two NMR Active Ti Isotopes by Static QCPMG Solid-State NMR Experiments*I Farnan*

University of Cambridge, Cambridge, United Kingdom

FH Larsen

University of Copenhagen, Copenhagen K, Denmark

Free Radical Processes in Gamma- and Heavy Ion Irradiated DNA*D Becker, MD Sevilla*

Oakland University, Rochester, Michigan

Probing Mechanisms of Novel Templated Synthesis*L Wang*

Pacific Northwest National Laboratory, Richland, Washington

Solid-State NMR and ENDOR Studies of Silica Polyamine Composites*E Rosenberg, DJ Nielsen*

University of Montana, Missoula, Montana

Pulsed EPR Studies of Transition Metal-Exchanged Zeolites and Molecular Sieves*SC Larsen, JF Woodworth*

University of Iowa, Iowa City, Iowa

Structure of Human Telomerase RNA*G Varani, TC Leeper*

University of Washington, Seattle, Washington

Mechanisms of Phosphorus Stabilization in the Soil Environment: A Molecular Scale Evaluation*S Hunger*

University of Delaware, Newark, Delaware

Ultra-High Field NMR Studies of Stable Isotope Applications*LA Silks*

Los Alamos National Laboratory, Los Alamos, New Mexico

Structural Characterization of p53, c-Myc and the Protein-Protein Interactions That Regulate Their Biological Activity*CH Arrowsmith*

University of Toronto, Toronto, Ontario, Canada

Multinuclear MAS NMR of Cesium Alumino-Silicate Compounds*MJ Lambregts*

University of Idaho, Idaho Falls, Idaho

Structural Proteomics: Annotating the Genome Using 3-D Structure*CH Arrowsmith, A Yee*

University of Toronto, Toronto, Ontario, Canada

Solid-State NMR Characterization of Metal Phosphines*JV Hanna*

Australian Nuclear Science & Technology Organization, Menai, New South Wales, Australia

Probing the Mechanism of the Alkaline Phosphatase Reaction by ^{67}Zn and ^{25}Mg NMR*ER Kantrowitz*

Boston College, Chestnut Hill, Massachusetts

Structural Biology of the DNA Repair Proteins: The Nudix Protein Family from the Extremely Radiation-Resistant Bacterium *Deinococcus radiodurans**DE Wemmer*

Lawrence Berkeley National Laboratory, University of California, Berkeley, California

High-Field NMR Studies of Very Large RNA Molecules: The VS Ribozyme*T Dieckmann, JC Flinders*

University of California Davis, Davis, California

Structure of a Helical Signaling Domain from Cas*KR Ely, K Briknarova*

The Burnham Institute, La Jolla, California

Aluminum Coordination Environments in Alumina*DA Lindquist, GG Burnside*

University of Arkansas, Little Rock, Arkansas

NMR Structure of Sec35p/Cog2p*FM Hughson, I Pelczar, L Cavanaugh*

Princeton University, Princeton, New Jersey

Interaction of *Escherichia coli* Formamidopyrimidine-DNA Glycosylase (Fpg) with Damaged DNA Containing an 7,8-Dihydro-8-oxoguanine Lesion*SS Wallace*

University of Vermont, Burlington, Vermont

Solid-State NMR Investigation of Coating Materials Prepared Using the SNAP Methodology*RA Mantz*

Air Force Research Laboratory, Wright Patterson Air Force Base, Ohio

Solution Al-27 NMR at 750 MHz (H1) of Methylaluminoxanes*LG Butler, JL Eilertsen, WD Treleaven*

Louisiana State University, Baton Rouge, Louisiana

Structural Determination of ApoLp-III/HDL Particles*J Wang, C Xu*

Southern Illinois University, Carbondale, Illinois

Structural Genomics of Eukaryotic Model Organisms*GT Montelione*

Rutgers University, Piscataway, New Jersey

Activation of the Arp2/3 Complex by WASP Family Proteins: Probing Individual Subunits by NMR*MK Rosen, M Kreishman-Detrick*

University of Texas Southwestern Medical Center, Dallas, Texas

NMR Structural Investigations of BRCA1*RE Klevit, PS Brzovic*

University of Washington, Seattle, Washington

Technique Development, Further Studies of Ultra-Stable Acid Zeolites, Investigations of AlPO₄ Materials, Studies of Ceramic Materials*CA Fyfe, AR Lewis, DH Brouwer*

University of British Columbia, Vancouver, British Columbia, Canada

Structure and Interactions of 25 kDa Dynein Light Chain Homodimer*EJ Barbar*

Ohio University, Athens, Ohio

Understanding Hepatitis B Infection: Structure of Hepatitis B Virus X Protein Bound to its Cellular Partner*KR Ely, K Briknarova*

The Burnham Institute, La Jolla, California

Solid-State NMR Spectroscopy of Half-Integer Spin Quadrupolar Nuclei at High Magnetic Field Strengths: A Continuing Study of Hydrochloride Salts and Zirconium Phosphates*KW Feindel, RE Wasylshen*

University of Alberta/Dalhousie University, Edmonton, Alberta, Canada

An Extended Study of Solid Prototypal Chromium and Molybdenum Compounds Using ^{53}Cr and ^{95}Mo Nuclear Magnetic Resonance Spectroscopy*MA Forgeron, KJ Ooms, RE Wasylshen*

University of Alberta/Dalhousie University, Edmonton, Alberta, Canada

Spatial Properties of Clustered Free Radicals Produced in DNA and Biosimulators by Ionizing Radiation*JD Zimbrick*

Purdue University, West Lafayette, Indiana

 ^{11}B MAS NMR Spectroscopy of Amorphous Metal Boride Hydrotreating Catalysts*ME Bussell, M Pease, J King, G Parks, SJ Sawhill, KA Layman, DR Van Wyk*

Western Washington University, Bellingham, Washington

Post Mortem Energy Metabolism and Water Characteristics in Rabbit *M. longissimus* Studied by Dynamic Slow-Speed MAS NMR Spectroscopy and Relaxometry*RA Wind*

Pacific Northwest National Laboratory, Richland, Washington

H Bertram, HJ Andersen

Danish Institute of Agricultural Sciences, Tjele, Denmark

EPR and ENDOR Characterization of Fe and Mn Containing Spin Systems of Relevance to Proteins, Magnetic Materials, and Oxidation Catalysts*SW Gordon-Wylie*

University of Vermont, Burlington, Vermont

NMR Analysis of Pyrrolidinone Precursors and Derivatives*JE Holladay, MA Lilga*

Pacific Northwest National Laboratory, Richland, Washington

AI-27 NMR Analysis of Lactate Media Containing Al Colloids*JE Amonette*

Pacific Northwest National Laboratory, Richland, Washington

Distance Measurements in RNA Using DEER Spectroscopy with Site-Directed Spin Labeling*N Kim, VJ DeRose*

Texas A&M University, College Station, Texas

NMR Investigation of Folding and Dynamics of the I κ B/NF κ B System*G Melacini, EA Komives*

University of California San Diego, La Jolla, California

Contrast-Enhanced ¹H-NMR of Microbial Biofilms*MJ Miller*

University of Notre Dame, Notre Dame, Indiana

Biofilm Studies Using Multi-Modal Molecular Imaging Agents*DJ Bornhop*

Texas Technical University, Lubbock, Texas

FJ Brockman

Pacific Northwest National Laboratory, Richland, Washington

Protonation State of Nicotine in Tobacco Smoke Particulate Matter by Solid-State NMR*DH Peyton*

Portland State University, Portland, Oregon

KC Barsanti

Oregon Health Sciences University/Oregon Graduate Institute, Beaverton, Oregon

Ge Crystal Orientation to Facilitate a Search for Dark Matter via the Majorana Neutrinoless Double-Beta Decay Experiment*KM Kazkaz, JF Wilkerson*

University of Washington, Seattle, Washington

NMR of Klaui Ligand Complexes*LA Snow, BK McNamara*

Pacific Northwest National Laboratory, Richland, Washington

Structure of Telomerase RNA*G Varani, TC Leeper*

University of Washington, Seattle, Washington

Probing Nanostructural Materials*L Wang*

Pacific Northwest National Laboratory, Richland, Washington

Investigating Molecular Recognition and Biological Function at Interfaces Using Antimicrobial and Biomineralization Peptides*ML Cotten, MN Manion, KC Daugherty*

Pacific Lutheran University, Tacoma, Washington

Development of Resolution Enhancement Techniques for the Complete Structure Determination of Fully $^{13}\text{C}/^{15}\text{N}$ -Labelled Peptides and Proteins Using Solid-State NMR*SK Straus*

University of British Columbia, Vancouver, British Columbia, Canada

Continuing Exploration of NMR Imaging of Microorganisms in Porous Media Using NMR Microscopy*BD Wood*

Oregon State University, Corvallis, Oregon

HE Trease

Pacific Northwest National Laboratory, Richland, Washington

Solid-State NMR Studies of Rhamnolipid Metal Complexes*CK Larive, WH Otto*

University of Kansas, Lawrence, Kansas

High-Field 1Q MAS and MQMAS Solid-State NMR Studies of the Dissolution of Montmorillonite Clays Under Alkaline Conditions*GS Crosson, KT Mueller*

Pennsylvania State University, University Park, Pennsylvania

Atomic-Level Investigations of Thermal Spring Deposits: S-NMR of Natural Siliceous Sinters*NW Hinman*

University of Montana, Missoula, Montana

Structure and Dynamics of MUC1 Immune Recognition: Significance for Breast Cancer Vaccine Design*AP Campbell, MD Diaz, JS Grinstead*

University of Washington, Seattle, Washington

Aluminum Coordination Environments in Lanthanum Stabilized Alumina and in Hydrotalcite*DA Lindquist, GG Burnside*

University of Arkansas, Little Rock, Arkansas

MUC1 Humoral Immune Recognition: Mapping Antibody-Tumor Associated Antigen Interactions*AP Campbell, JS Grinstead*

University of Washington, Seattle, Washington

NMR Characterization of Spider Silk Proteins and the Effect of Processing on Spider Silk Films*RA Mantz, RA Vaia, MO Stone*

Air Force Research Laboratory, Wright Patterson Air Force Base, Ohio

Structural Characterization of Free and Fibronectin-Bound Anastellin*KR Ely, K Briknarova*

The Burnham Institute, La Jolla, California

Structural Biology of DNA Repair Proteins: The Nudix Protein Family from the Extremely Radiation-Resistant Bacterium *Deinococcus radiodurans**GW Buchko, MA Kennedy*

Pacific Northwest National Laboratory, Richland, Washington

SR Holbrook

Lawrence Berkeley National Laboratory, University of California, Berkeley, California

Imaging Beta Amyloid Plaques in a Transgenic Mouse Model of Alzheimers Disease*JF Quinn*

Oregon Health Sciences University/Oregon Graduate Institute, Portland, Oregon

Structural Biology of Mammalian Chromatin High Mobility Group Protein HMGA1 and UV-Damaged DNA*MJ Smerdon*

Washington State University, Pullman, Washington

GW Buchko, MA Kennedy

Pacific Northwest National Laboratory, Richland, Washington

Crystal Orientation Determination of a Piezoelectric Crystal*MB Toloczko*

Pacific Northwest National Laboratory, Richland, Washington

Structural Genomics of Eukaryotic Model Organisms*JM Aramini, GT Montelione*

Rutgers University, Piscataway, New Jersey

Variable-Temperature MAS NMR Spectroscopic Study of Incorporated and Sorbed ¹³³Cs and ²³Na in Zeolitic Minerals*Y Deng, M Flury*

Washington State University, Pullman, Washington

Separation of ⁴⁷Ti and ⁴⁹Ti Solid-State NMR Lineshapes from Crystalline and Glassy Materials by Static QCPMG Experiments*I Farnan*

University of Cambridge, Cambridge, United Kingdom

FH Larsen

University of Copenhagen, Copenhagen, Denmark

Defect Dynamics on Crystalline Quartz*JJ Weil, SM Botis, SM Nohbrin*

University of Saskatchewan, Saskatoon, Saskatchewan, Canada

Structure Determination of Membrane Proteins*FD Soennichsen, K Choowongkamon*

Case Western Reserve University, Cleveland, Ohio

Structural Investigations of Solid Materials by High-Resolution Solid-State NMR at Very High Field*CA Fyfe, DH Brouwer, CM Schneider*

University of British Columbia, Vancouver, British Columbia, Canada

High-Field Solid-State ^{99}Ru NMR Spectroscopy in Inorganic and Organometallic Ruthenium Compounds*RE Wasylshen, KJ Ooms*

University of Alberta/Dalhousie University, Edmonton, Alberta, Canada

An Extended Study of Solid Molybdenum and Organometallic Magnesium Compounds Using ^{95}Mo and ^{25}Mg Nuclear Magnetic Resonance Spectroscopy*RE Wasylshen, MA Forgeron, KJ Ooms*

University of Alberta/Dalhousie University, Edmonton, Alberta, Canada

Electron Paramagnetic Resonance of Non-Heme Iron Proteins*PS Covello, M Loewen*

National Research Council/Plant Biotechnology Institute, Saskatoon, Saskatchewan, Canada

Metabonomics Assessment Following ANIT or Acetaminophen Administration to Male Fischer 344 Rats*DF Lowry*

Pacific Northwest National Laboratory, Richland, Washington

AF Fuciarelli

Battelle Columbus, Richland, Washington

Structure and Sequence Determination of Simple Dipeptides by Nuclear Magnetic Resonance Spectroscopy*AG Cavinato*

Eastern Oregon University, La Grande, Oregon

NMR of Small Organics*TC Squier, MU Mayer-Cumblidge*

Pacific Northwest National Laboratory, Richland, Washington

Microscopic Characterization of Porosity, Diffusivity, and Tortuosity in Single Particles of Hanford Sediments Using Nuclear Magnetic Resonance (NMR) Technique

C Liu

Pacific Northwest National Laboratory, Richland, Washington

Quantifying the Intracellular Spatial State and Dynamics of Water, Macromolecule Interactions: Studies of Living Cells

B Franza, RK Kong

University of Washington, Seattle, Washington

Using NMR to Identify Potential Geometric Isomers of Metal Chelate Systems

DB Rodovsky, LS Sapochak

Pacific Northwest National Laboratory, Richland, Washington

Interaction of Solution-State Silicates with Trivalent Cations

HM Cho, AR Felmy, OS Qafoku, Y Xia

Pacific Northwest National Laboratory, Richland, Washington

Special Purpose Re-Configurable ASIC Hardware for Accelerating Protein Structure Analysis Software

TJ Conroy

University of Regina, Regina, Saskatchewan, Canada

Structural Studies of SecA ATPase, a Critical Component of Protein Translocation Machinery

C Kalodimos, N Biris

Rutgers University, Newark, New Jersey

Investigating the Heterogeneity of Polymer Aging

BR Cherry, TM Alam

Sandia National Laboratories, Albuquerque, New Mexico

Structural Studies of the Hyaluronan Receptor CD-44 and CD44-HA Complex

R Michalczyk, NH Pawley

Los Alamos National Laboratory, Los Alamos, New Mexico

Structural Genomics of Eukaryotic Model Organisms

JM Aramini, GT Montelione

Rutgers University, Piscataway, New Jersey

Structure of the PR Domain of RIZ1 Tumor Suppressor

KR Ely, K Briknarova

The Burnham Institute, La Jolla, California

Structure Determination of Membrane Proteins*FD Soennichsen, K Choowongkamon*

Case Western Reserve University, Cleveland, Ohio

NMR Structural Studies of apoAI/preb-HDL Particles*J Wang, X Ren, C Xu, D Fan*

Southern Illinois University, Carbondale, Illinois

Structural Investigations of Solid Materials by High Resolution Solid-State NMR at Very High Field*CA Fyfe, CM Schneider*

University of British Columbia, Vancouver, British Columbia, Canada

Solid-State NMR Studies on Structures and Oxidation Behavior of Amorphous SiAlCN Ceramics*L An*

University of Central Florida, Orlando, Florida

Interaction of *Escherichia coli* Formamidopyrimidine-DNA Glycosylase (Fpg) with Damaged DNA Containing an 7,8-Dihydro-8-oxoguanine Lesion*SS Wallace*

University of Vermont, Burlington, Vermont

GW Buchko, MA Kennedy

Pacific Northwest National Laboratory, Richland, Washington

TRAPDOR Experiments on Siliceous Sinters from Thermal Springs*NW Hinman*

University of Montana, Missoula, Montana

Complexation of Th(IV) by Organic Acids in Aqueous Solution*HM Cho, AR Felmy*

Pacific Northwest National Laboratory, Richland, Washington

Kinetics of Polyphosphate Decomposition in Heterogeneous Environments*BK McNamara, DM Wellman*

Pacific Northwest National Laboratory, Richland, Washington

Staff

David W. Hoyt, Senior Research Scientist, Technical Lead
(509) 373-9825, david.w.hoyt@pnl.gov

Araceli Perez, Administrative Assistant
(509) 376-2548, araceli.perez@pnl.gov

Sarah D. Burton, Senior Research Scientist
(509) 376-1264, sarah.burton@pnl.gov

Joseph J. Ford, Senior Research Scientist
(509) 376-2446, joseph.ford@pnl.gov

Michael J. Froehlke, Technician V
(509) 376-2391, michael.froehlke@pnl.gov

Nancy G. Isern, Research Scientist
(509) 376-1616, nancy.isern@pnl.gov

Donald N. Rommereim, Senior Research Scientist
(509) 376-2671, don.rommereim@pnl.gov

Jesse A. Sears, Technician VI
(509) 376-7808, jesse.sears@pnl.gov